

Probing nuclear activity versus star formation at $z \sim 0.8$ using near-infrared multiobject spectroscopy

C. Ramos Almeida^{1,2*}, J. M. Rodríguez Espinosa^{1,2}, J. A. Acosta-Pulido^{1,2}, A. Alonso-Herrero^{3,4}, A. M. Pérez García^{1,2}, N. Rodríguez-Eugenio^{1,2}

¹*Instituto de Astrofísica de Canarias (IAC), C/Vía Láctea, s/n, E-38205, La Laguna, Tenerife, Spain*

²*Departamento de Astrofísica, Universidad de La Laguna, E-38205, La Laguna, Tenerife, Spain*

³*Instituto de Física de Cantabria, CSIC-Universidad de Cantabria, E-39005 Santander, Spain*

⁴*Augusto González Linares Senior Research Fellow*

ABSTRACT

We present near-infrared (NIR) spectroscopic observations of 28 X-ray and mid-infrared selected sources at a median redshift of $z \sim 0.8$ in the Extended Groth Strip (EGS). To date this is the largest compilation of NIR spectra of active galactic nuclei (AGN) at this redshift. The data were obtained using the multi-object spectroscopic mode of the Long-slit Intermediate Resolution Infrared Spectrograph (LIRIS) at the 4.2 m William Herschel Telescope (WHT). These galaxies are representative of a larger sample studied in a previous work, consisting of over a hundred X-ray selected sources with mid-infrared counterparts, which were classified either as *AGN-dominated* or *host galaxy-dominated*, depending on the shape of their spectral energy distributions (SEDs). Here we present new NIR spectra of 13 and 15 sources of each class respectively. We detect the H α line at $\geq 1.5\sigma$ above the continuum for the majority of the galaxies. Using attenuation-corrected H α luminosities and observed Spitzer/MIPS 24 μm fluxes, and after subtracting an AGN component estimated using an AGN empirical correlation and multifrequency SED fits, we obtain average star formation rates (SFRs) of 7 ± 7 and $20 \pm 50 M_{\odot} \text{ yr}^{-1}$ respectively (median SFRs = 7 and 5 $M_{\odot} \text{ yr}^{-1}$). These values are lower than the SFRs reported in the literature for different samples of non-active star-forming galaxies of similar stellar masses and redshifts ($M_{*} \sim 10^{11} M_{\odot}$ and $z \sim 1$). In spite of the small size of the sample studied here, as well as the uncertainty affecting the AGN-corrected SFRs, we speculate with the possibility of AGN quenching the star formation in galaxies at $z \sim 0.8$. Alternatively, we might be seeing a delay between the offset of the star formation and AGN activity, as observed in the local universe.

Key words: galaxies:active – galaxies:nuclei – galaxies:starburst – infrared:galaxies.

1 INTRODUCTION

The role of active galactic nuclei (AGN) in the formation and evolution of galaxies is still not well established. It is not clear whether AGN represent episodic phenomena in the life of galaxies, are random processes (given that the supermassive black hole is already there, at least in the local universe), or are more fundamental. Some authors claim that AGN are key in quenching the star formation in their host galaxies through the so-called AGN feedback (see e.g. Granato et al. 2004; Ho 2005; Springel et al. 2005; Schawinski et al. 2007, 2009). This “negative” AGN feedback has been invoked to explain the well-established cor-

relations between supermassive black hole (SMBH) mass and host galaxy properties (e.g. Kormendy & Richstone 1995; Magorrian et al. 1998; Ferrarese & Merritt 2000; Gebhardt et al. 2000; Greene & Ho 2006). A similar correlation has been observed in starburst galaxies, in which bright stellar clusters, also called Central Massive Objects (CMO), take the role of the SMBH (Ferrarese et al. 2006; Wehner & Harris 2006).

In order to understand the importance of the AGN feedback in the evolution and the star formation histories of galaxies, it is necessary to study how the star formation rate (SFR) in active galaxies evolve with redshift. AGN at cosmological distances have been widely studied in the optical due to the relatively high number of multi-object spectrographs in this range. On the other hand, the sparse number of these instruments in the NIR translates

* E-mail: cra@iac.es

in the lack of spectroscopic studies of distant AGN in the NIR. This range offers the opportunity to study the optical spectra of galaxies at $z \sim 1$. At this redshift, the $H\alpha$ line is shifted into the J-band. This recombination line is a good tracer of the instantaneous SFR, since it is proportional to the ionising UV Lyman continuum radiation from young and massive stars and it has little dependence on metallicity (Kennicutt 1998; Bicker & Fritze-v. Alvensleben 2005). Characterising the SFRs of active galaxies using either $H\alpha$ or any other indicator (e.g. the IR emission) is very challenging, as the AGN contributes to both the continuum and the emission line spectrum. Thus, estimates of the SFRs of powerful AGN, as for example quasars, will be contaminated with AGN emission to a certain extent. On the other hand, the SFRs of deeply buried and optically-dull AGN obtained from $H\alpha$ emission may only have a small contribution from the AGN. These optically-dull AGN are defined as X-ray-selected AGN with no evidence for nuclear accretion activity in optical spectroscopy, showing stellar emission-dominated or obscured optical-to-infrared SEDs instead, practically indistinguishable from those of spiral/starburst galaxies (Alonso-Herrero et al. 2004, 2008; Rigby et al. 2006; Trump et al. 2009).

The star formation activity in the hosts of AGN at $z \sim 1$ has been studied by several authors using mid-infrared (MIR), far-infrared (FIR), and submillimeter data (Alonso-Herrero et al. 2008; Bundy et al. 2008; Brusa et al. 2009; Lutz et al. 2010; Santini et al. 2012). The latter authors found that the period of moderately luminous AGN activity does not seem to have strong influence in the star formation activity of the galaxies, in contradiction with the results found at low redshift (e.g. Ho 2005). For example, based on FIR data from the Herschel Space Observatory, Santini et al. (2012) reported evidence of an enhancement on the star formation activity in the host galaxies of a sample of X-ray-selected AGN at $0.5 < z < 2.5$, as compared to a mass-matched control sample of non-active galaxies. However, when they only considered star-forming galaxies in the control sample (i.e. they discarded quiescent galaxies), they found roughly the same level of star formation as in the AGN hosts. A similar result was found by Lutz et al. (2010), based on submillimeter data of a sample of 895 X-ray selected AGN at $z \sim 1$, for which they measured a $SFR \sim 30 M_{\odot} yr^{-1}$. This value, which they estimated assuming star formation-dominated submillimeter emission, is among the typical SFRs found for samples of non-active star-forming galaxies at $z \sim 1$ and $M_{*} \gtrsim 10^{10.5} M_{\odot}$ (e.g. Noeske et al. 2007). Alonso-Herrero et al. (2008) studied the star formation properties of 58 X-ray-selected AGN at $0.5 < z < 1.4$ by modelling their multifrequency SEDs and did not find strong evidence for either highly suppressed or enhanced star formation when compared to a mass-matched sample of galaxies at the same redshift. However, these AGN were selected to have SEDs dominated by stellar emission, and thus, they are representative of only 50% of the X-ray-selected AGN population.

In our previous work (Ramos Almeida et al. 2009; hereafter RA09) we fitted the optical to MIR SEDs of a sample of 116 X-ray-selected AGN in the Extended Groth Strip (EGS) with different starburst, AGN, and galaxy templates from Polletta et al. (2007). Based on this SED fitting, we classified them as AGN-dominated (52%) and host galaxy-

dominated (48%) objects. The latter have SEDs typical of starburst, spiral, or elliptical galaxies, indicating the presence of a deeply buried or a low-luminosity AGN. From our SED fits, we derived photometric redshifts for all the galaxies, which range from $z_{phot}=0.05$ to 3. By dividing the sample according to the fitted templates, in RA09 we proposed an evolutionary sequence, similar to the one suggested for early-type galaxies by Schawinski et al. (2007): an intense period of star formation would be quenched by AGN feedback as the BH accretes enough mass, competing for the cold gas reservoir and heating it, and becoming dominant. The AGN-phase would then continue through lower ionization phases, ending as spiral or elliptical galaxies hosting low-luminosity AGN.

This paper constitutes a spectroscopic follow-up of a representative subset of the AGN sample studied in RA09. These AGN were selected in the X-rays and all of them have MIR counterparts (i.e. detection in the 3.6, 4.5, 5.8, 8, and 24 μm bands of the Spitzer Space Telescope). See Section 2 for further details in the sample selection. Here we present NIR spectroscopic observations for 28 of these AGN, which have spectroscopic redshifts in the range $z=[0.27, 1.28]$, and a median redshift of $z=0.76$. These objects are representative of the whole sample in terms of redshift, magnitude, and SED types (see Section 2), including 13 AGN-dominated and 15 host galaxy-dominated objects. The main goals of this work are first, to classify the galaxies spectroscopically to check the reliability of the SED classification done in RA09, and second, obtain SFRs using the $H\alpha$ emission. We will compare these SFRs with those obtained using Spitzer 24 μm observed fluxes. Throughout this paper we assume a cosmology with $H_0 = 75 km s^{-1} Mpc^{-1}$, $\Omega_m=0.27$, and $\Omega_{\Lambda}=0.73$.

2 SAMPLE AND PHOTOMETRIC DATA

The AGN sample studied in RA09 was originally selected by Barmby et al. (2006) in the X-rays, using Chandra data from Nandra et al. (2005) and XMM-Newton data from Waskett et al. (2004). Barmby et al. (2006) considered only the 152 X-ray sources lying within the boundaries of the Spitzer observations with a limiting full-band flux (0.5-10 keV) of $2 \times 10^{-15} ergs^{-1} cm^{-2}$ in the case of the XMM-Newton data, and of $3.5 \times 10^{-16} ergs^{-1} cm^{-2}$ for the Chandra data. At the flux limits of these X-ray surveys, most of the sources are expected to be AGN and have $\log(f_X/f_{opt}) > -1$, indicating that they are not quiescent (i.e. non-active) galaxies. Finally, they selected the 138 objects with secure detections in the four Spitzer/IRAC bands (3.6, 4.5, 5.8, and 8 μm) and Spitzer/MIPS 24 μm band.

In addition to the X-ray and MIR data, in RA09 we used optical and NIR archival data from the AEGIS project¹ (Davis et al. 2007) to increase the coverage of the AGN SEDs. All the fluxes employed in RA09 were directly retrieved from the *Rainbow Cosmological Surveys*

¹ The AEGIS project is a collaborative effort to obtain both deep imaging covering all major wavebands from X-ray to radio and optical spectroscopy over a large area of sky. <http://aegis.ucolick.org/index.html>

database², which is a compilation of photometric and spectroscopic data, jointly with value-added products such as photometric redshifts and synthetic rest-frame magnitudes, for several deep cosmological fields (Pérez-González et al. 2008; Barro et al. 2009, 2011). Of the 138 sources in the Barmby et al. (2006) sample, we discarded 42 galaxies that showed multiple detections in the ground-based images (optical and NIR) to avoid source confusion in the Spitzer MIR fluxes.

To classify the observed SEDs and estimate photometric redshifts, we combined optical data from the Canada-France-Hawaii Telescope Legacy Survey (CFHTLS; u,g,r,i,z) T0003 worldwide release (Gwyn 2012); NIR fluxes (J and K_S) from the version 3.3 of the Palomar-WIRC K-selected catalog (Bundy et al. 2006), and Spitzer MIR data (IRAC 3.6, 4.5, 5.8, 8 μ m and MIPS 24 μ m) from Barmby et al. (2006). We fitted these SEDs with the library of starburst, AGN, and galaxy templates from Polletta et al. (2007) using the photometric redshift code HyperZ (Bolzonella et al. 2000). The templates span the wavelength range 0.1–1000 μ m. See RA09 for a detailed description of the data, photometric redshift calculations, and SED classification.

The galaxies were then classified in five main categories in terms of the template used to fit their SEDs³:

(i) *Starburst-dominated*. Includes several templates of starburst galaxies (e.g. M82-like) and ultraluminous infrared galaxies (ULIRGs) with starburst (e.g. Arp 220-like).

(ii) *Starburst-contaminated*. Comprises three different starburst-composite SEDs: one starburst/Seyfert 1 and two starburst/Seyfert 2.

(iii) *Type-1*. Includes three Type-1 quasar (QSO) SEDs.

(iv) *Type-2*. Consists of two Type-2 QSOs, a Seyfert 2 and a Seyfert 1.8 SED.

(v) *Normal galaxy*. Includes the SEDs of three elliptical galaxies and seven spirals of different types.

Our main goal in RA09 was to classify the galaxies into these five groups and study their properties. It is worth clarifying that all of the sources are, in principle, AGN, on the basis of their X-ray and MIR emission, but only those included in the *Type-1*, *Type-2* and *Starburst-contaminated* (*SB-cont*) groups have AGN-dominated SEDs. On the other hand, those included in the *Starburst-dominated* (*SB-dom*) group have their SEDs dominated by starburst emission from the optical to the MIR. Finally, the *Normal galaxy* (*NG*) are weak AGN embedded in an otherwise elliptical or spiral galaxy emission.

It is possible, however, that a small fraction of the sample are star-forming galaxies emitting in the X-rays and MIR (see e.g. Pereira-Santaella et al. 2011; Ranalli et al. 2012). In order to confirm the dominance/presence of the AGN over the star formation/host galaxy emission and vice versa, and to estimate SFRs from the H α emission, we obtained NIR spectroscopic data for a subsample of 28 galaxies ($\sim 30\%$ of the total sample), which are representative of the five groups described above (see Table 1). In the following, we will refer

to these 28 sources as AGN, although one of the goals of this work is to confirm the presence of nuclear activity.

In order to discard any possible bias in redshift and/or magnitude, in Figure 1 we show histograms for the observed subsample and the whole RA09 sample. According to the Kolmogorov-Smirnov (KS) test, there is no significant difference between the two samples in terms of observed magnitude and redshift at the 2σ level.

In Figure 2 we show the observed galaxy SEDs and the templates fitted in RA09 to classify them in the previously mentioned groups, as well as to estimate photometric redshifts. The fits are the same presented in RA09, with the exception of those of the galaxies G17, G57, G78, and G105. We repeated these four fits because the photometric redshifts were not compatible with the spectroscopic redshifts derived from the NIR spectra presented here ($|z_{NIR} - z_{phot}| > 0.2$). We performed the fits using HyperZ and restricting the input redshift range to $z_{NIR} \pm 0.08$, which is the maximum difference between z_{NIR} and z_{phot} found for the rest of the sample observed with LIRIS. This sample includes 5 *SB-dom*, 2 *SB-cont*, 3 *Type-1*, 8 *Type-2*, and 10 *NG*, which were selected to cover the five SED groups and to maximize the number of targets in the LIRIS multi-slit masks (see Section 3.1).

Color-composite images obtained with the Advanced Camera for Surveys (ACS) on the Hubble Space Telescope (HST) for the 18 galaxies with data available in the AEGIS website⁴ are shown in Figure 3. The *Type-1* G63 and G78 show blue colors and strong point sources, while galaxies classified as either *Type-2* (e.g. G53) or *SB-dom* (e.g. G55 and G62) show obscured nuclei. Examples of spiral galaxies are G74 and G107, which were fitted with spiral templates in RA09. Finally, the morphology of G36 resembles that of an elliptical galaxy with a strong dust lane crossing the nucleus.

3 OBSERVATIONS AND DATA REDUCTION

3.1 NIR spectroscopy

NIR spectroscopic observations of the subsample of 28 galaxies selected from RA09 were obtained from 2008 March to 2009 May using the multi-object spectroscopic (MOS) mode of the NIR camera/spectrometer LIRIS (Manchado et al. 2004). LIRIS is attached to the Cassegrain focus of the 4.2 m WHT and it is equipped with a Rockwell Hawaii 1024 x 1024 HgCdTe array detector. The spatial scale is 0.25'' pixel⁻¹.

Four masks were designed to observe a representative subset of the five groups described in Section 2. The galaxies were selected by their RA and Dec., to maximize the number of targets per mask. Details of each mask and the journal of observations are reported in Table 2. The chosen slit-width was 0.85'', with the lengths varying between 8.5'' and 12'', allowing enough space for nodding while avoiding overlap of the spectra. We used the low-resolution grism ZJ, which covers the range 0.8–1.4 μ m, providing a spectral resolution of ~ 500 km s⁻¹ with the 0.85'' slits. The spectral range varies depending on the position of the slits on the mask along the spectral direction. Thus, a slit in the center of the

² https://rainbowx.fis.ucm.es/Rainbow_Database

³ http://www.iasf-milano.inaf.it/~polletta/templates/swire_templates.html

⁴ <http://tkserver.keck.hawaii.edu/egs/>

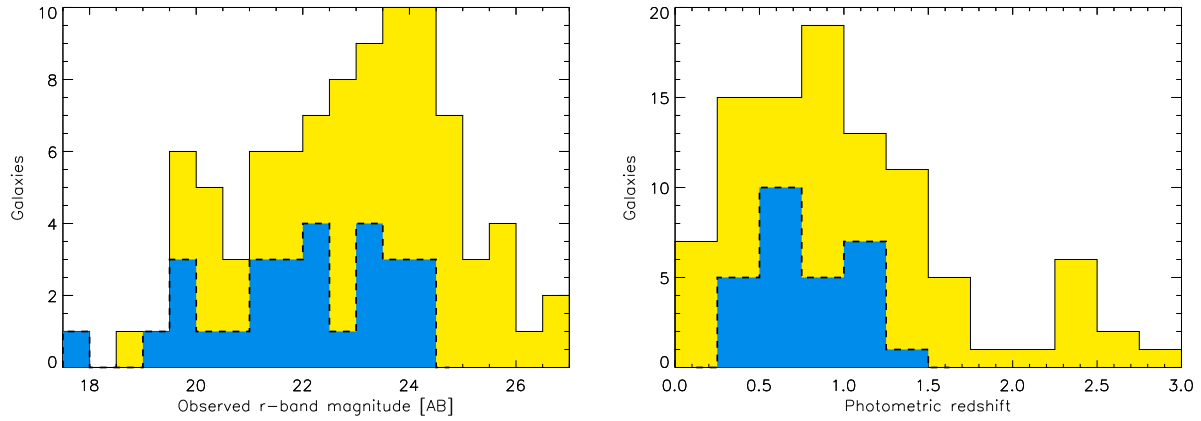


Figure 1. Left panel: observed r-band magnitudes for the whole AGN sample studied in RA09 (yellow and continuous line histogram) and for the subsample of 28 galaxies observed with LIRIS (blue and dashed line histogram). Right panel: same as in the left panel, but for the photometric redshift distributions.

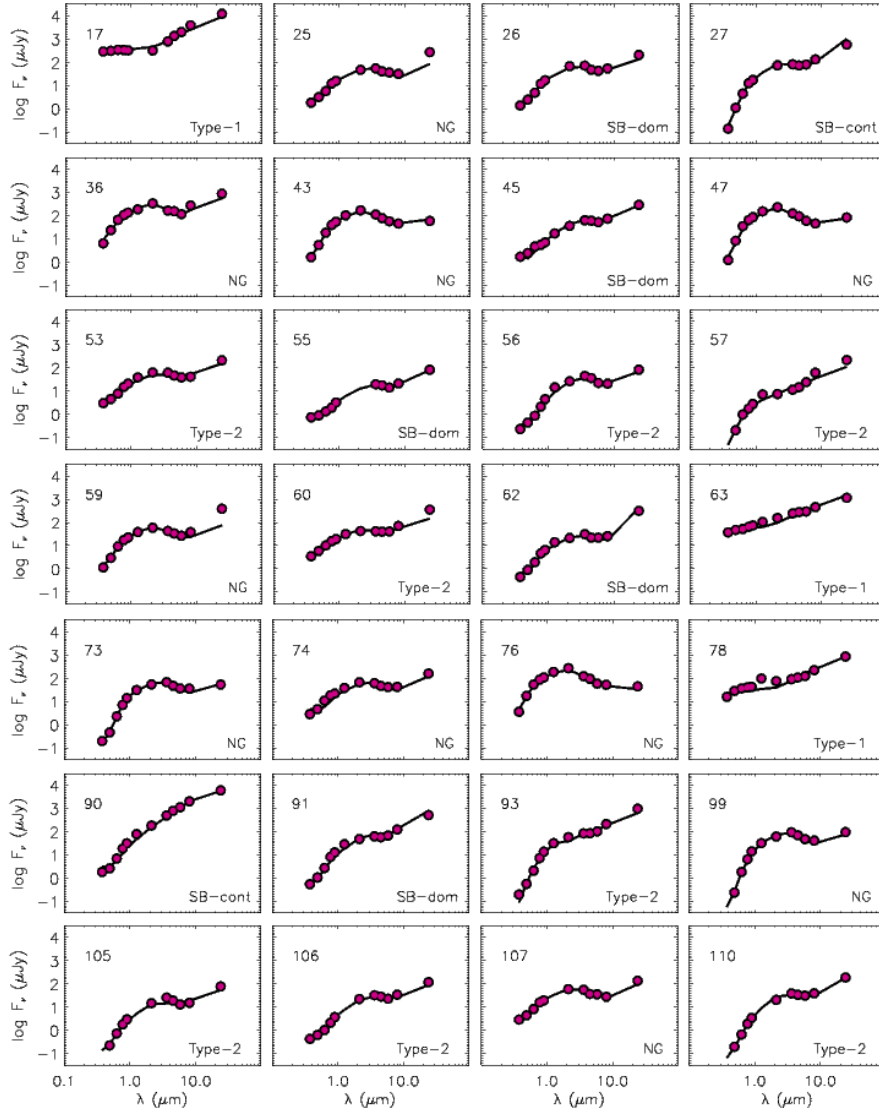


Figure 2. Observed SEDs (dots) of the subsample of 28 AGN observed with LIRIS, fitted with the AGN, starburst, and composite templates from Polletta et al. (2007), using HyperZ. The SED group and galaxy ID from RA09 are indicated in each panel.

ID	ID DEEP2	RA (°)	Dec (°)	J (AB)	Log (L_X)	z_{spec}	z_{phot}	Group
G17	11039094	214.1768	52.3034	[17.41]	44.53	1.284 (a)	1.25	3
G25	11038472	214.2065	52.2815	[20.40]	42.97	0.761 (4)	0.75	5
G26	11038492	214.2079	52.3025	[20.27]	43.37	0.808 (4)	0.73	1
G27	11038266	214.2104	52.2763	[20.00]	43.45	0.683 (4)	0.60	2
G36	12004450	214.2675	52.4149	18.22	42.52	0.281 (4)	0.25	5
G43	12008608	214.2870	52.4525	18.87	42.08	0.532 (4)	0.47	5
G45	12008576	214.2940	52.4747	20.81	43.59	-	1.25	1
G47	12004491	214.2961	52.4280	18.44	≤ 41.79	0.418 (b)	0.34	5
G53	12004467	214.3134	52.4474	19.94	43.13	0.723 (4)	0.67	4
G55	12008051	214.3290	52.4623	[21.93]	≤ 43.03	1.211 (3)	1.23	1
G56	12008091	214.3303	52.4655	21.01	42.92	1.208 (3)	1.19	4
G57	12004011	214.3335	52.4168	21.77	42.71	-	0.70	4
G59	12012474	214.3456	52.5288	19.93	42.06	0.465 (4)	0.46	5
G60	12012471	214.3475	52.5316	20.14	42.68	0.484 (4)	0.50	4
G62	12012431	214.3510	52.5416	21.02	≤ 42.55	0.902 (4)	0.83	1
G63	12008225	214.3525	52.5069	18.84	43.31	0.482 (4)	0.54	3
G73	12012467	214.3859	52.5342	20.18	43.61	0.986 (4)	0.91	5
G74	12012543	214.3909	52.5637	19.95	42.70	0.551 (4)	0.52	5
G76	12012534	214.3932	52.5186	18.22	41.48	0.271 (4)	0.29	5
G78	12008222	214.3998	52.5083	18.93	44.66	0.985 (c)	1.04	3
G90	12007954	214.4244	52.4732	19.16	44.40	1.148 (4)	1.15	2
G91	12007926	214.4393	52.4976	20.25	43.33	0.873 (4)	0.87	1
G93	12007878	214.4415	52.5091	20.14	43.89	0.985 (3)	0.97	4
G99	12007962	214.4550	52.4676	20.13	42.88	0.996 (4)	1.00	5
G105	...	214.4657	52.5129	[22.10]	41.87	-	0.57	4
G106	12007949	214.4684	52.4814	[21.69]	43.22	-	1.00	4
G107	12007896	214.4707	52.4775	[20.10]	≤ 42.04	0.671 (3)	0.60	5
G110	12012132	214.4760	52.5232	[21.51]	42.56	-	0.65	4

Table 1. Columns 1 and 2 list the ID from Barnby et al. (2006) and from the DEEP2 database. Columns 3, 4, and 5 give the IRAC 3.6 μm right ascension and declination and the J mag from the Palomar-WIRC K-selected catalog. For the galaxies lacking of Palomar J mags, values from the SED fits are given between brackets instead. Column 6 lists the observed hard X-ray luminosities from Nandra et al. (2005) and Waskett et al. (2004) in erg s^{-1} . Column 7 lists the spectroscopic redshift from DEEP2 when available (reliability is given between brackets: 3=robust and 4=very robust) and from other literature sources for the galaxies G17, G47, and G78. Columns 8 and 9 list the photometric redshift and the SED classification from RA09 (1 = SB-dom; 2 = SB-cont; 3 = Type-1; 4 = Type-2; 5 = NG). Refs: (a) Schneider et al. (2005); (b) Steidel et al. (2003); (c) Lilly et al. (1995).

mask will provide a spectrum in the nominal spectral range (0.8–1.4 μm), whereas spectra obtained with slits closer to the edges of the mask will be shifted either bluewards or redwards.

In addition to the science targets slitlets (see details in Table 2), each mask contained an extra-slit, designed to simultaneously obtain the spectrum of a star of ~ 16 –17 mag in the J-band (AB). These stars, which are brighter than the science targets (see Table 1), allowed, on the one hand, to ensure that the masks were well-centred during the observation (the majority of the targets are too faint to be detected in single exposures), and on the other hand, to calculate the corresponding correction once the spectra were flux-calibrated.

We performed the observations following an ABCABC telescope-nodding pattern, placing the source in three positions along the slit, using an offset of 3'' around the central position of the pattern (B). Individual frames of 600 s in each nodding position were taken (see Table 2), amounting a total integration time of 3600 s per ABCABC pattern, and a total of four hours per mask. Re-centering of the masks was done every hour, since the relative position between the star used for guiding and the science targets might have changed

due to differential atmospheric refraction. The wavelength calibration was provided by observation of the argon lamp available in the calibration unit at the A&G box of the telescope. To obtain the telluric correction and the flux calibration for each galaxy, the nearby G0 stars HD136674 and HD115269 were observed before and after the science targets. Spectra of the two stars were obtained through three slitlets covering the whole wavelength coverage.

We reduced the data following standard procedures for NIR spectroscopy, using the *lirisdr*⁵ dedicated software within the IRAF⁶ environment. For the MOS mode, the available routines use a-priori mask design information to trace the slitlets positions and limits in a uniformly illuminated frame. We did not perform flat-field correction after checking that, at least in the case of our observations, it only introduced additional noise. We subtracted the mean of alternate pairs (A+C)/2 of two-dimensional spectra from that

⁵ <http://www.iac.es/project/LIRIS>

⁶ IRAF is distributed by the National Optical Astronomy Observatory, which is operated by the Association of Universities for the Research in Astronomy, Inc., under cooperative agreement with the National Science Foundation (<http://iraf.noao.edu/>).

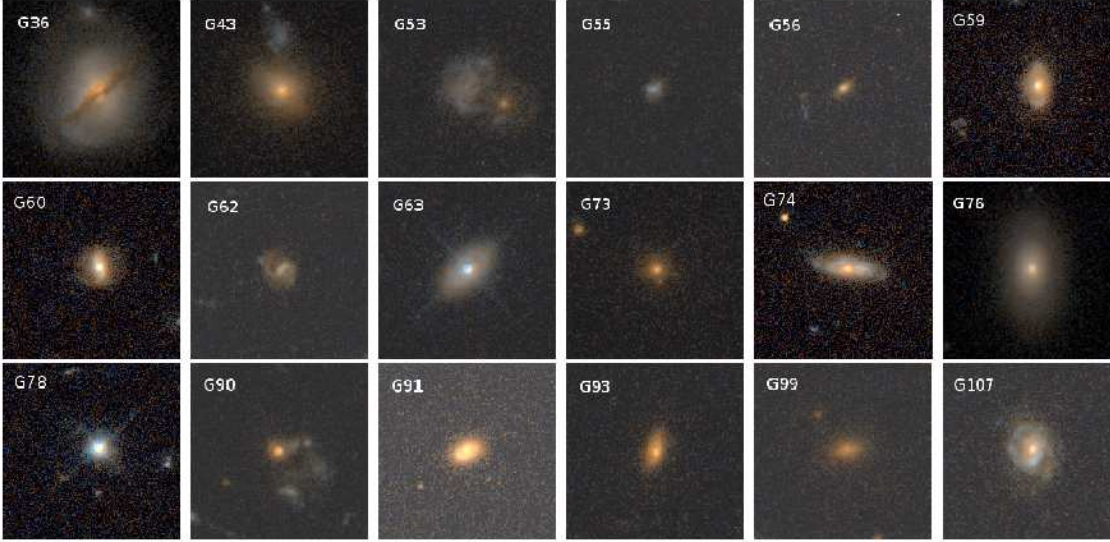


Figure 3. ACS/HST color-composite images of the 18 AGN in our LIRIS representative sample lying in the AEGIS ACS fields. Images are 7 arcsec size and were downloaded from the AEGIS website (<http://tkserver.keck.hawaii.edu/egs/egs.php>). North is up and East is left.

Mask	Slits	Position	P.A.	Obs. Date	Exposure Time	Airmass	Seeing
EGS1	8	214.375, +52.535	5°	2008 Mar 28	4x6x600 s	1.09-1.35	~1''
EGS2	8	214.293, +52.446	9°	2009 May 9	4x6x600 s	1.09-1.28	~0.6''
EGS3	8	214.458, +52.498	26°	2009 May 8	4x6x600 s	1.09-1.41	~0.7-0.9''
EGS5	4	214.182, +52.283	26°	2009 May 8,9	2x6x600 s	1.55-1.98	~0.6-0.7''

Table 2. Summary of the NIR multi-object spectroscopic observations

taken in the B position of the nodding pattern to remove the sky background. The resulting frames were wavelength-calibrated before registering and co-adding all frames to provide the final spectra.

We then extracted the individual spectra for each galaxy and reference star, using an aperture of 1'', matching the maximum value of the seeing during the observations (see Table 2). We finally divided the extracted spectra by the corresponding G0 star spectrum to remove telluric contamination. We used a modified version of *Xtellecor* (Vacca et al. 2003) in this step, which provides both the telluric correction and the flux calibration.

We estimated the uncertainties in the galaxy fluxes due to slit-losses for each mask using the reference stars, observed with the extra-slitlet mentioned above. We finally corrected the fluxes of the science targets by applying a correction factor to the individual spectra. The observed NIR spectra of the 28 AGN are shown in Figures 4 to 10. We have represented the observed J-band fluxes calculated from the Palomar-WIRC magnitudes reported in Table 1 for comparison with our flux-calibrated spectra. The Palomar fluxes were calculated in apertures of 2'' diameter (Bundy et al. 2006) and thus correspond to total fluxes for the majority of the galaxies in the sample (see Figure 3). Consequently, these J-band fluxes should be equal or higher than the flux-calibrated LIRIS nuclear spectra, as indeed happens for all the galaxies. This gives us extra-confidence in our

flux-calibration. For those galaxies without Palomar J-band magnitudes available (see Table 1), values from the SED fits shown in Figure 2 are given instead, and are represented as open diamonds.

The largest differences between the J-band photometry and spectroscopy are found for the galaxies G36, G43, and G47. The three of them are *NG* according to our SED fits, which are in agreement with their early-type morphologies, at least for G36 and G43 (those with ACS images available; see Figure 3). Thus, the nuclear flux of these objects (the spectra were extracted using apertures of 1'') will not be the dominant contribution to the total flux, as opposed to the AGN-dominated galaxies. In addition, the three galaxies have relatively low redshifts: $z = [0.28, 0.53]$, making more different their nuclear and total emission. For example, 1'' at $z=0.3$ and 0.8 corresponds to 4.2 and 7.1 kpc respectively.

3.2 DEEP optical spectroscopy

As indicated in Table 1, for 20 of the galaxies in the sample observed with LIRIS there are publicly available spectroscopic data from the Deep Extragalactic Evolutionary Probe 2 (DEEP2; Davis et al. 2003). The spectra were obtained during 80 nights between 2002 and 2005 using the DEIMOS multiobject spectrograph (Faber et al. 2003) on the Keck-II telescope, which provides a spectral resolution $R = \lambda/\Delta\lambda \sim 5000$ covering the nominal range 6400-9100

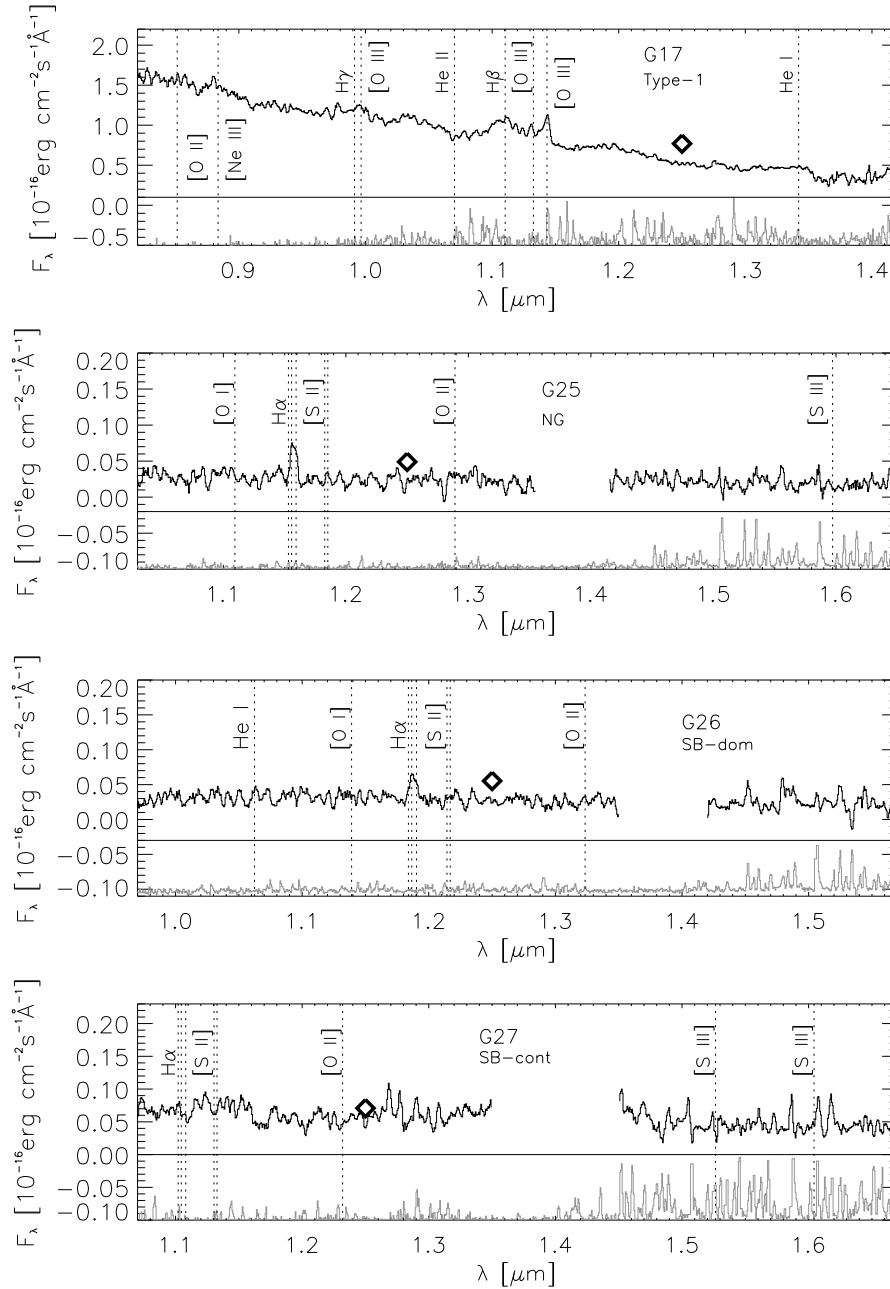


Figure 4. Observed NIR LIRIS spectra of the galaxies G17, G25, G26, and G27. Typical AGN emission lines are labelled. The H α labels correspond to H α +2[N II]. The SED classification from RA09 is indicated at the top of each panel, and a scaled sky spectrum for each galaxy is plotted at the bottom. Observed J-band fluxes from the magnitudes reported in Table 1 are represented with a cross for comparison. Open diamonds correspond to the J-band fluxes from the SED fits shown in Figure 2.

Å. DEEP2 employed a slit width of $1''$, providing a spectral resolution of 1.4 \AA and dispersion of $0.3 \text{ \AA pixel}^{-1}$ (Davis et al. 2007). The reduced and extracted spectra were retrieved from the Keck website⁷ and they correspond to the Data Release 3 (DR3)⁸. Note that the Data Release 4 has recently become public (Newman et al. 2012), but we have checked that there are no changes in the spectra of

our galaxies. Thus, here we use the DR3 integrated spectra extracted along the locus of constant λ , following Horne (1986), and corrected for the effects of tilted slits.

The DEEP2 spectra are not flux calibrated and do not have the same spatial resolution as the LIRIS data. However, this can be solved by individually scaling the optical spectra to the averaged continuum flux of the overlapping (or bluest) NIR spectra. The 20 flux-calibrated optical spectra are presented in Appendix A. Our main interest in having optical spectra of our galaxies is to measure H β fluxes for those galaxies with H α detected in the NIR, and thus deter-

⁷ <http://tkserver.keck.hawaii.edu/egs/>

⁸ <http://deep.berkeley.edu/DR3/>

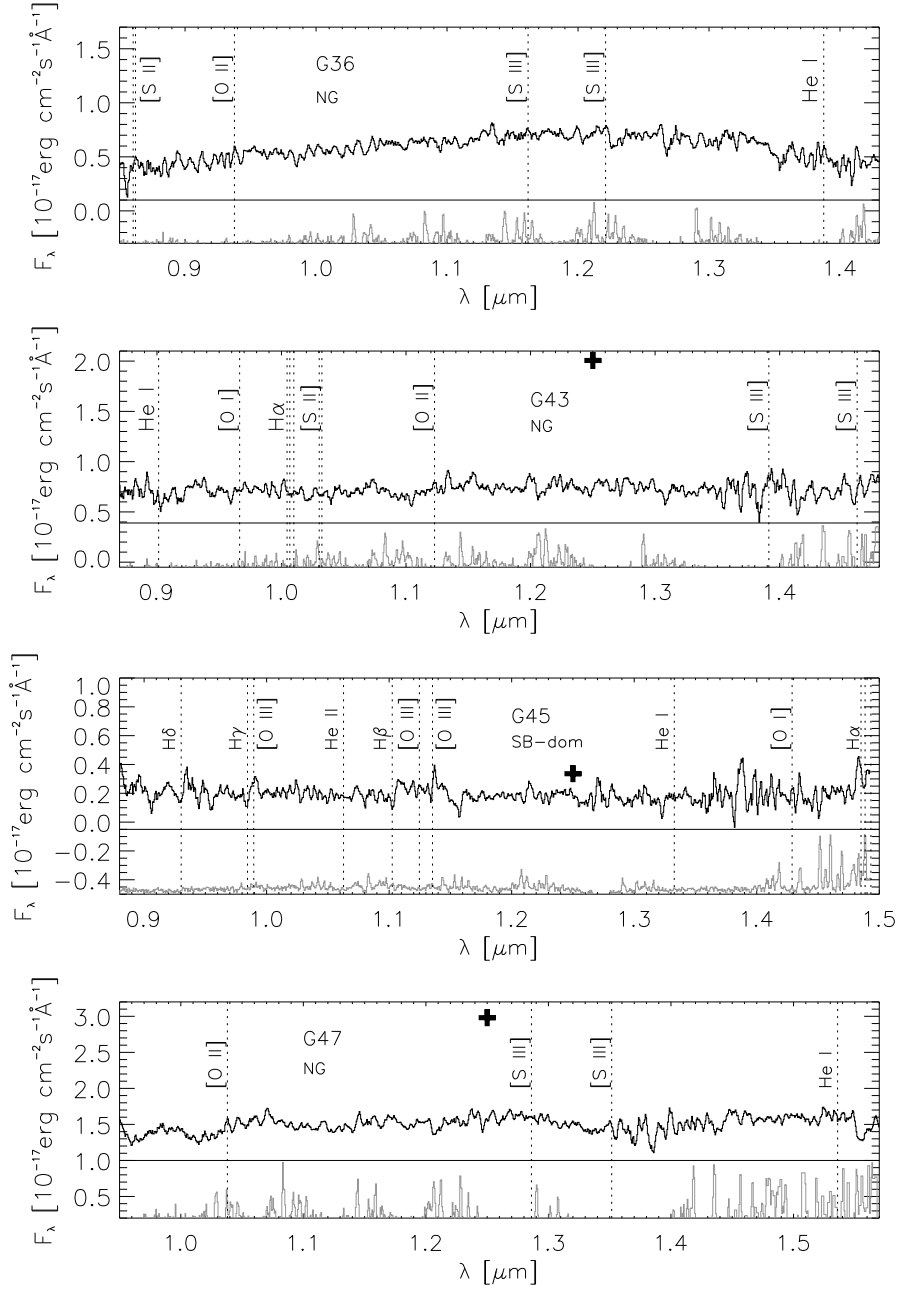


Figure 5. Same as in Figure 4 but for the galaxies G36, G43, G45, and G47. The J-band flux of the galaxy G36 is out of scale (J flux = $3.65 \times 10^{-17} \text{ erg cm}^{-2} \text{ s}^{-1} \text{ \AA}^{-1}$).

mine individual values of the extinction to correct our H α fluxes.

4 RESULTS

The NIR spectra of the sample observed with LIRIS show a wide variety of spectral features, including:

- (i) prominent emission lines typical of AGN and/or star forming galaxies (e.g. G17, G53, G55, G60, G78, and G90).
- (ii) H α detected in absorption (G43 and G76).
- (iii) Very weak emission lines or featureless spectra (e.g. G36, G99, and G106).

- (iv) Double-peaked emission lines corresponding to different kinematic components (G63).

After scaling the DEEP2 spectra to the flux-calibrated LIRIS data, we measured the fluxes of the emission lines. We fitted Gaussian profiles using the Starlink program DIPSO. The resulting emission line fluxes and FWHMs of H α , [N II] $\lambda 6584 \text{ \AA}$, H β , and [O III] $\lambda\lambda 4959, 5007 \text{ \AA}$ are reported in Table 3. Same but for other detected transitions, such as [O I] $\lambda 6300 \text{ \AA}$, [O II] $\lambda 3727, 7320 \text{ \AA}$, [O III] $\lambda 4363 \text{ \AA}$, and [S II] $\lambda 6732 \text{ \AA}$ is shown in Table 4. The line flux errors reported in Tables 3 and 4 are those given by DIPSO, and they include the uncertainty associated to the fit. All the line fluxes

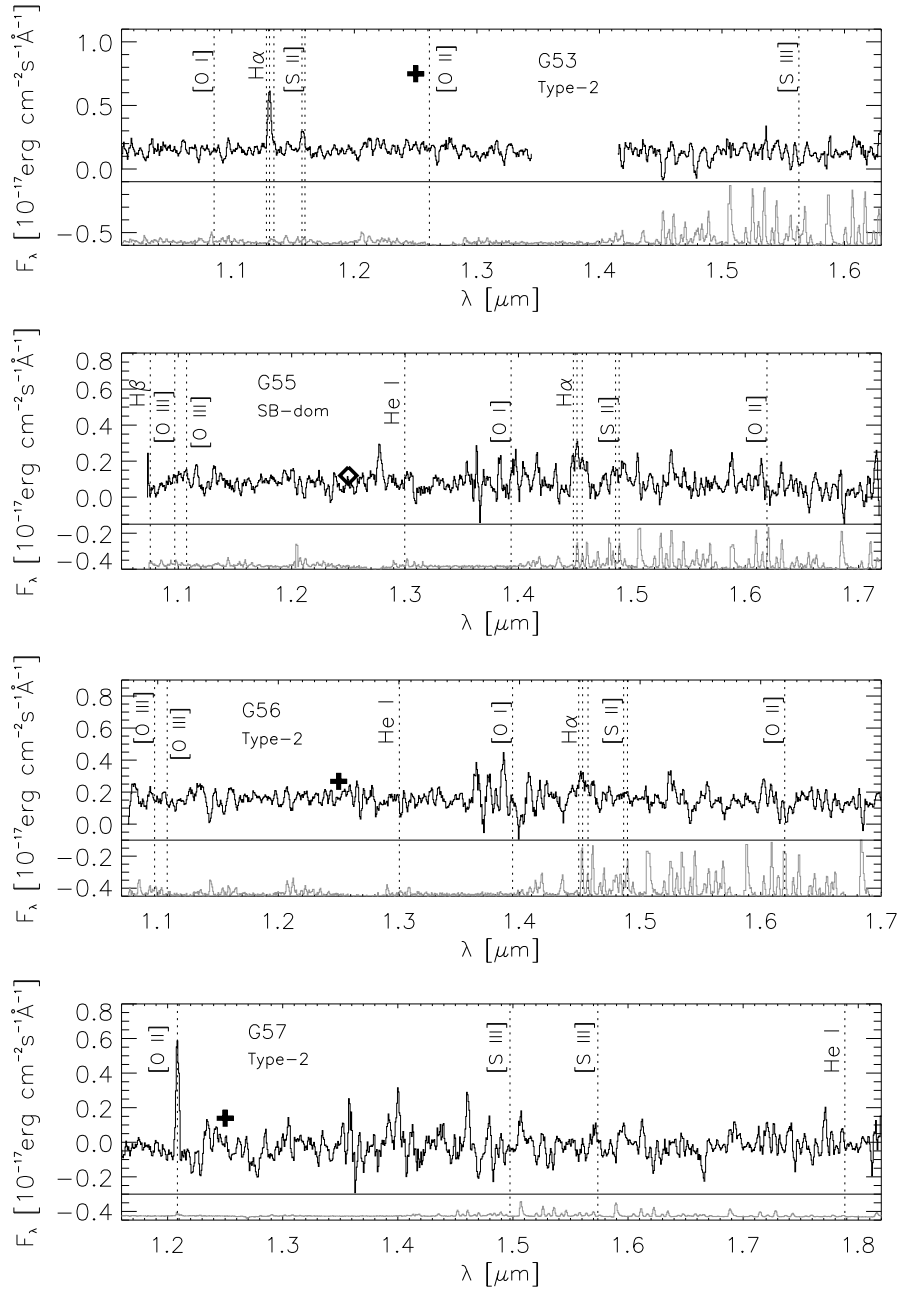


Figure 6. Same as in Figure 4 but for the galaxies G53, G55, G56, and G57.

reported correspond to detections at $\geq 1.5\sigma$ above the continuum noise, which we calculated as in Twite et al. (2012). We measure the continuum level and noise in two regions of ~ 200 Å adjacent to a given emission line, and then calculate the $1.5 \times \sigma \times FWHM$ flux (hereafter 1.5σ) above the continuum. Emission line fluxes larger than that are quoted in Tables 3 and 4, otherwise we report an upper limit equal to the 1.5σ flux. The exception are the sources lacking a secure spectroscopic redshift (G45, G57, G105, G106 and G110), for which a larger detection significance of 2σ is required.

The majority of the emission lines are well reproduced with a single Gaussian of FWHM typical of the narrow-line region (NLR; $\lesssim 1000$ km s $^{-1}$). For seven of the galaxies, namely G17, G55, G60, G63, G78, G90, and G107, an ad-

ditional broad Gaussian component was needed to reproduce the observed line profiles of the permitted lines. The majority of these broad components have FWHM $\gtrsim 2000$ km s $^{-1}$, typical of lines originated in the broad-line region (BLR). However, for some of the galaxies, intermediate-width components have been fitted instead (FWHM ~ 1000 – 1500 km s $^{-1}$).

Finally, in some cases it was necessary to fit two Gaussians to reproduce the profiles of the narrow lines in the DEEP2 spectra, of higher spectral resolution than the LIRIS data. This is the case of the galaxies G53, G55, G62, G63, G74, G93 and G99. In the LIRIS spectrum of G63, the double component of the H α line is clearly resolved as well (see Figure 7).

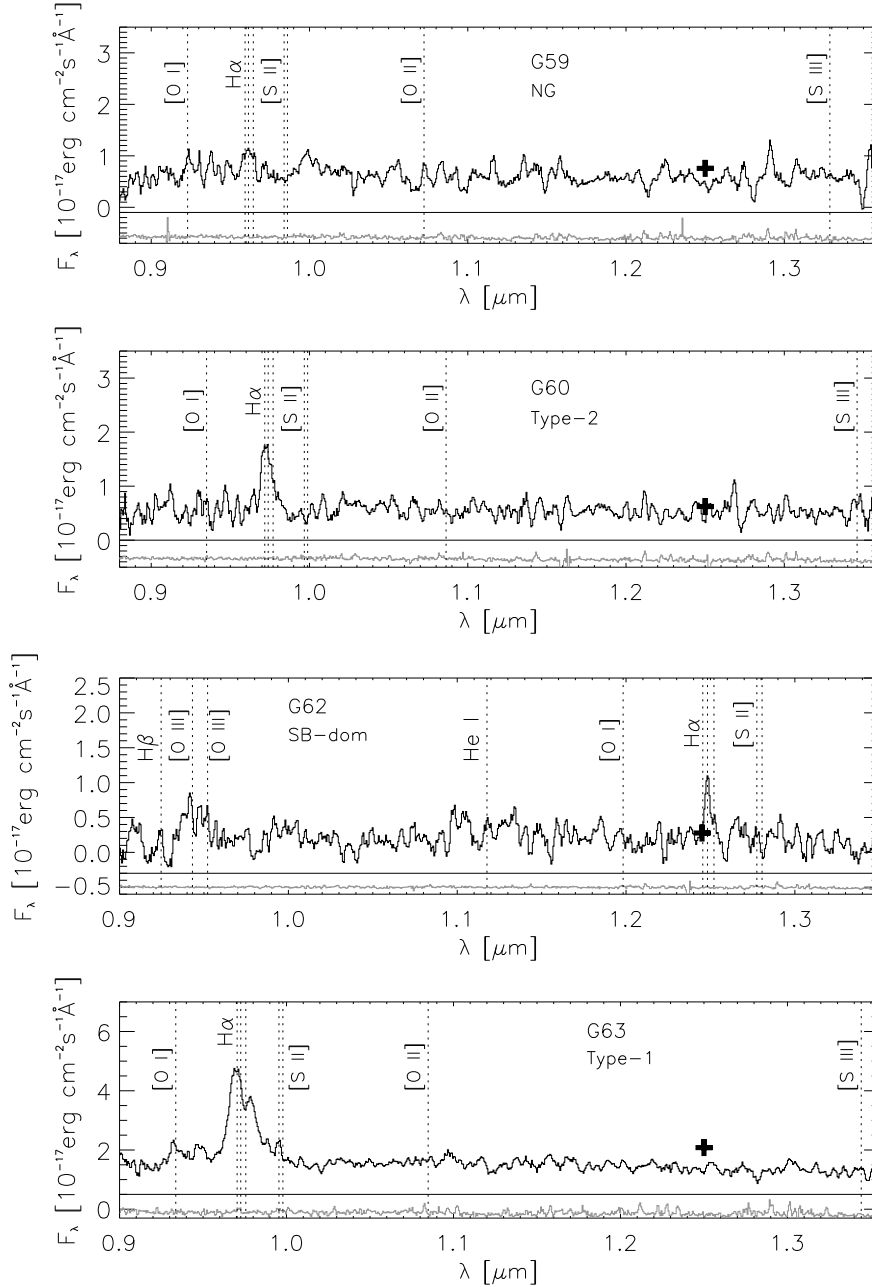


Figure 7. Same as in Figure 4 but for the galaxies G59, G60, G62, and G63.

In Figures 4 to 10 we show a sky spectrum for each of the galaxies, extracted using the same aperture as for the nuclear spectra. Although the sky lines are removed from the spectra of the targets, as we described in Section 3.1, residual noise could be affecting the emission line fluxes reported in Tables 3 and 4. In particular, the galaxies whose $H\alpha$ emission can be somehow affected by contamination of sky lines are G45, G55, G56, G90, G91, G93, G99, and G106.

4.1 Comparison between SED-fitting and spectral classification

On the basis of the spectroscopic features detected for the 28 galaxies observed with LIRIS, we can classify them spec-

troscopically to compare with the SED classification and to confirm the presence of nuclear activity. In Table 5 we summarize the results from this comparison.

First, we have to confirm the presence of nuclear activity in all the sources. At the flux limits of the X-ray surveys from which the sources were selected, most of the galaxies are expected to be AGN and have $\text{Log}(f_X/f_{opt}) > -1$, indicating that they are not quiescent (i.e. non-active) galaxies. Thus, in RA09 we assumed that all the X-ray/MIR sources were AGN. However, it is also possible that some of them are simply star-forming galaxies emitting in the X-ray. Thus, considering that here we have spectroscopic information for 28 galaxies, in addition to the SED classification and X-ray luminosities, it is worth confirming that they are AGN.

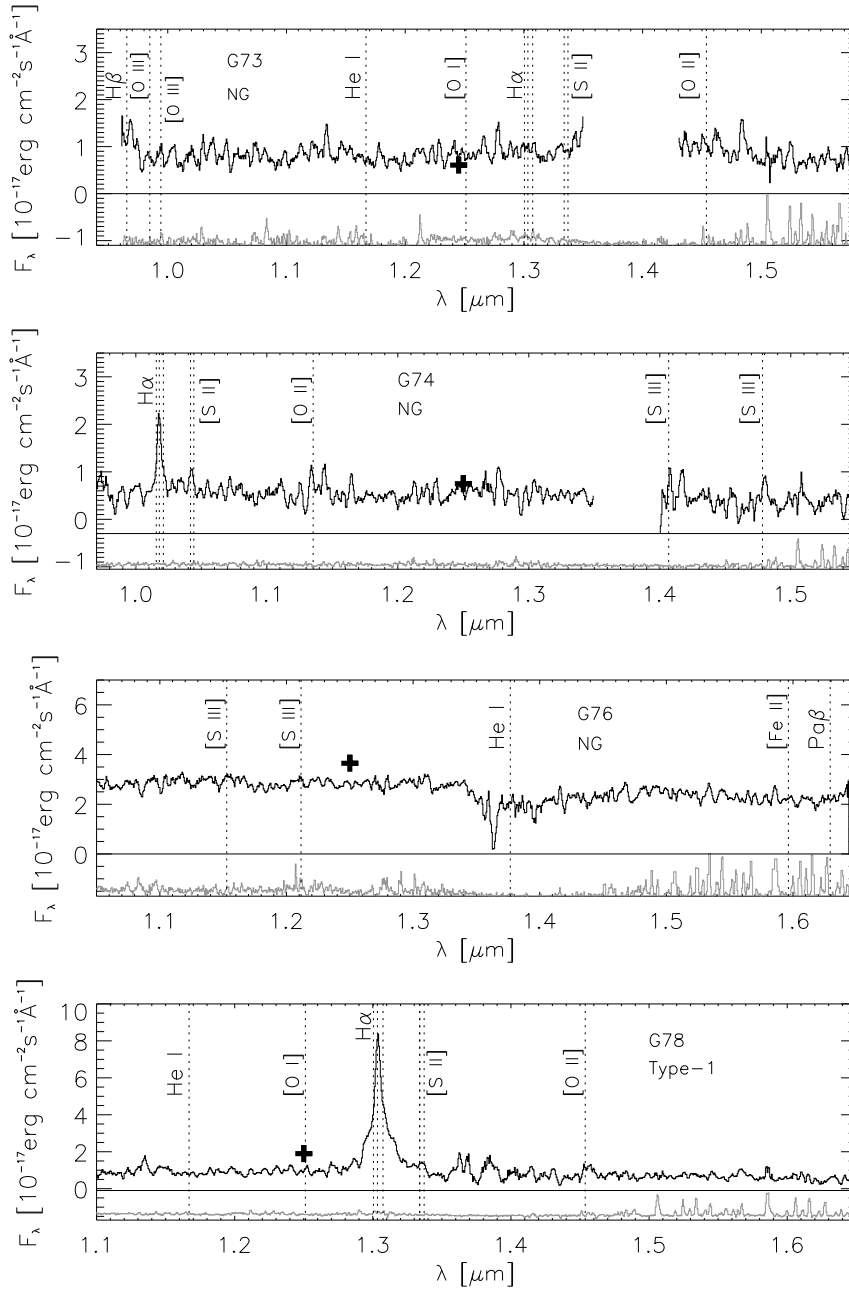


Figure 8. Same as in Figure 4 but for the galaxies G73, G74, G76, and G78.

The first thing to check are the hard X-ray luminosities. According to Ranalli et al. (2012), the criterium for a secure AGN origin of the X-ray luminosity is $L_X > 10^{42} (1+z)^{2.7} \text{ erg s}^{-1} = L_X^{AGN}$. However, this criterium is extremely restrictive, since it ignores the existence of low-luminosity AGN. As an example, in Pereira-Santaella et al. (2011) the authors studied the X-ray emission of a sample of 27 local luminous infrared galaxies (LIRGs) and found that the largest 2-10 keV luminosity was $2 \times 10^{41} \text{ erg s}^{-1}$. Such L_X corresponds to a LIRG that is forming stars at a rate of $92 M_\odot \text{ yr}^{-1}$. Only 8/28 sources have $L_X < L_X^{AGN}$, namely G43, G47, G55, G59, G62, G76, G105 and G107. Thus, for these galaxies, either their X-ray and MIR emission are due to intense star formation, or to a heavily obscured AGN.

Secondly, we will contrast the previous information with the spectroscopic and SED classifications. The three galaxies fitted with *Type-1* templates (G17, G63, and G78; see Figure 2) show broad components in their optical and/or NIR spectra. In fact, these are the only three galaxies with broad lines of $\text{FWHM} > 3000 \text{ km s}^{-1}$. G90 shows broad $\text{H}\alpha$ and $\text{H}\beta$ components of $\text{FWHM} \sim 1800 \text{ km s}^{-1}$, in agreement with its SED classification as a *SB-cont*: the fitted template for this galaxy is a Sy1/starburst/ULIRG SED. On the other hand, there are another three galaxies with broad lines detected in their spectra (G55, G60, and G107) which were not classified as *Type-1* AGN from their SED fits. Note, however, that those broad components have $\text{FWHMs} \lesssim 1500 \text{ km s}^{-1}$, and the luminosities of their broad $\text{H}\alpha$ components are con-

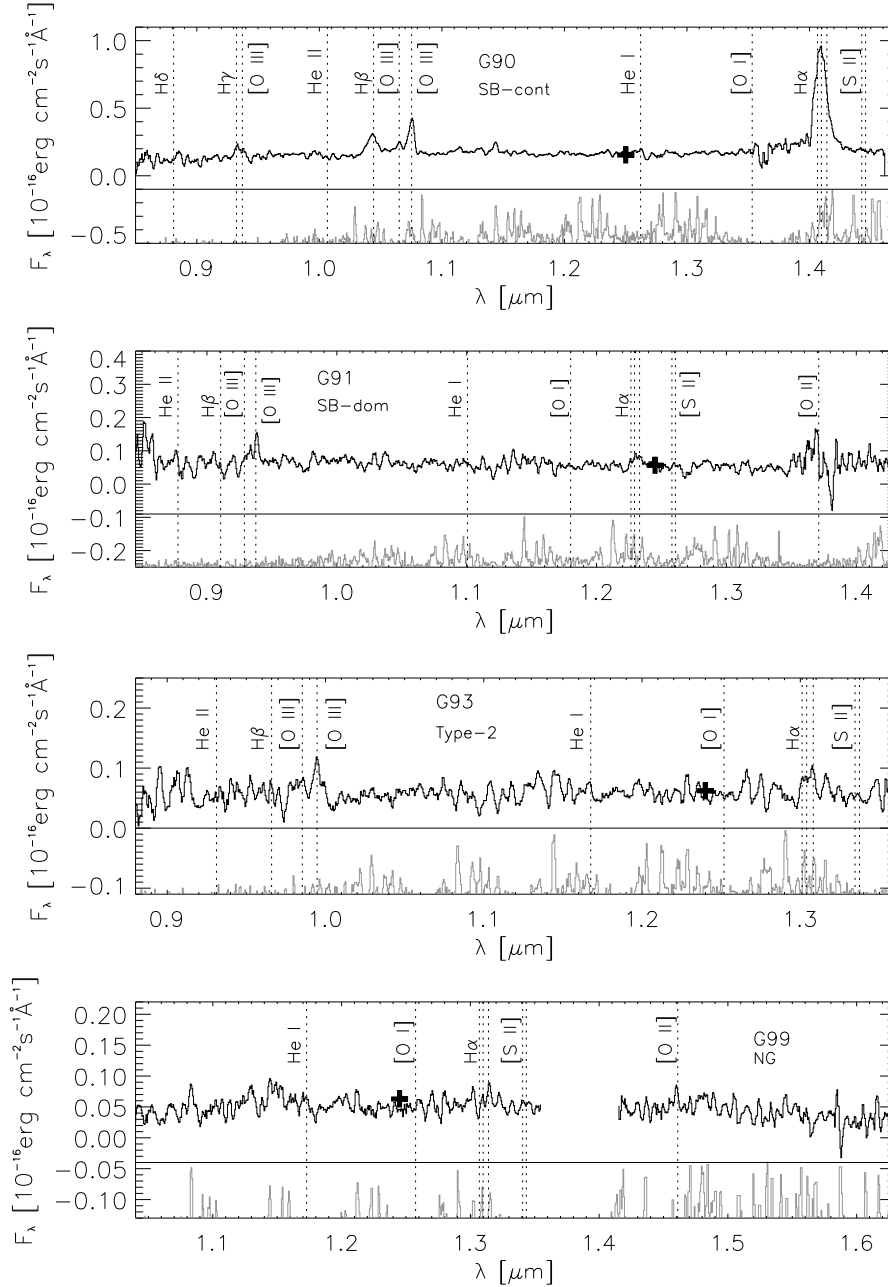


Figure 9. Same as in Figure 4 but for the galaxies G90, G91, G93, and G99.

siderably lower than those of the galaxies G63, G78, and G90, as we show in Table 5. In fact, broad $H\alpha$ emission is also detected in starburst galaxies (up to 2200 km s^{-1} in the case of stellar winds or supernovae remnants; see e.g. Boyle et al. 1995; Homeier et al. 1999; Westmoquette et al. 2011). Thus, G55 and G107 could be either normal galaxies with intense star formation, or heavily obscured Type-1 AGN.

For G43 and G76 we detect $H\alpha$ in absorption (as well as $H\beta$ in the case of G43), which is characteristic of early-type galaxies. This agrees with our SED classification as *NG* (see Table 5) and shows how deeply buried –or possibly absent– these AGN are. Of the other galaxies classified in this group, some of them show narrow permitted lines (G25, G36, G59,

and G74) and the rest have either very faint emission lines or practically featureless spectra (G47, G73, and G99).

The galaxies classified as *SB-dom* (G26, G45, G62, and G91) show very similar spectra, with relatively faint $H\alpha$ emission and $H\beta$ either in absorption or detected with very low signal-to-noise. Finally, the galaxies fitted with *Type-2* templates show narrow emission lines (G53, G56, G57, G93, G105, G106, and G110), as well as the *SB-cont* G27, whose SED was fitted with a Seyfert 2/starburst template in RA09.

To definitely confirm the agreement between the SED and spectroscopic classifications, we have plotted the line fluxes reported in Table 3 in a Baldwin-Phillips-Terlevich (BPT) diagram (Baldwin et al. 1981). In Figure 11 we show

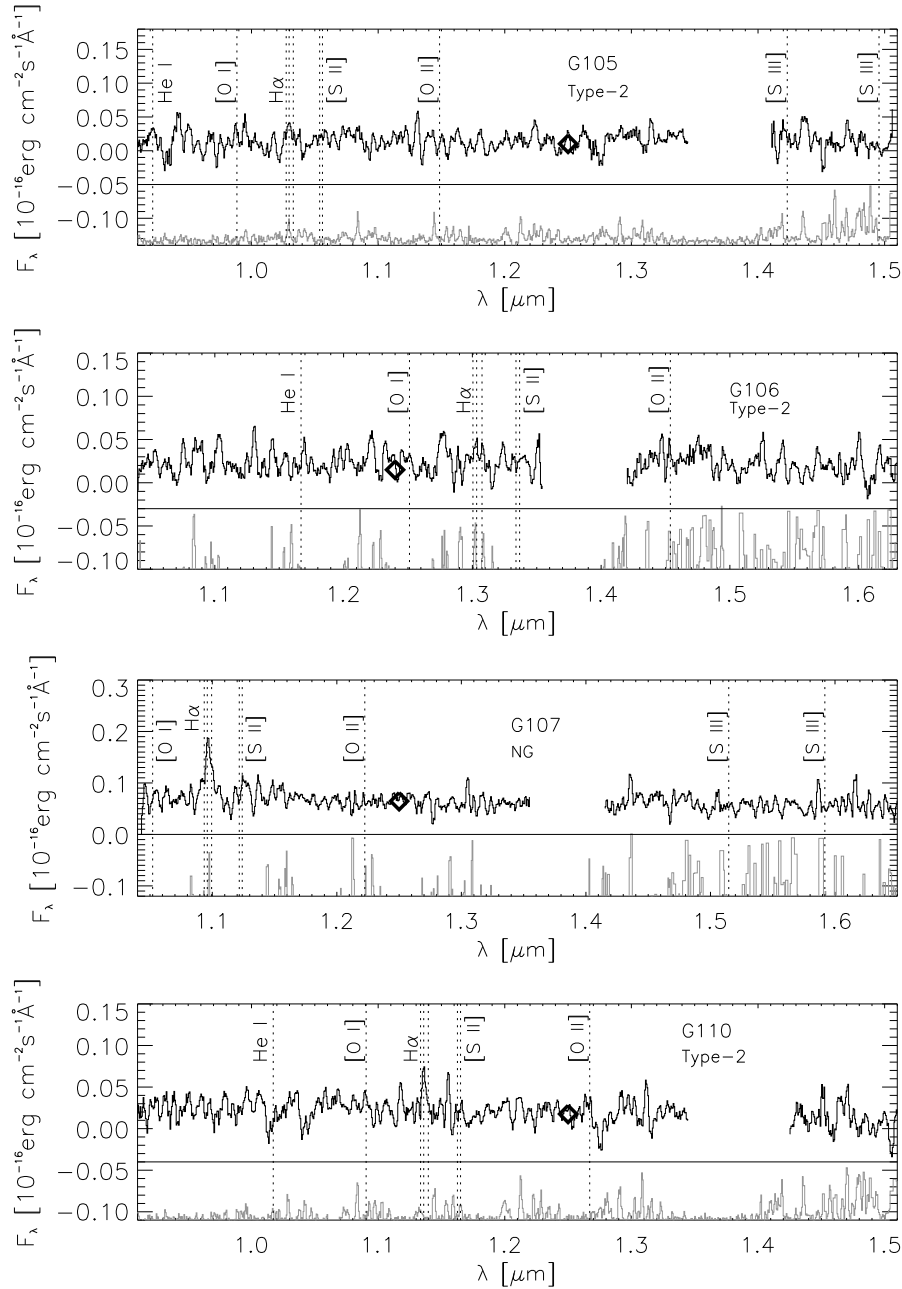


Figure 10. Same as in Figure 4 but for the galaxies G105, G106, G107, and G110.

the $[\text{O III}]\lambda 5007/H\beta$ versus $[\text{N II}]\lambda 6584/H\alpha$ ratios for the 11 galaxies in our sample with the four emission lines involved detected. Despite the low number of galaxies represented in this BPT diagram, examples of the five SED groups are included. Note that we have only considered the fluxes of the narrow-line components in this figure. The empirical separations between AGN and H II regions (dashed line = Kewley et al. 2001; solid line = Kauffmann et al. 2003) are shown together with the boundaries between LINERs and Seyfert galaxies ($[\text{O III}]/H\beta=3$ and $[\text{N II}]/H\alpha=0.6$; Kewley et al. 2006).

As expected, the *Type-1* G63 and the *SB-cont* G90 are well above the H II region. The *Type-2s* G60 and G93 also lie in the AGN region of the diagram, but with ratios more

typical of the Seyfert/LINER transition zone. G60 shows broad H α and H β components in its spectrum, but appears much closer to the boundary between the H II and AGN regions than, for example, G63. The galaxy G107, which shows broad components in its recombination lines, although with FWHMs $\sim 900 \text{ km s}^{-1}$ only, is located in the composite region between the Kauffmann et al. (2003) and Kewley et al. (2006) definitions. This agrees with our SED classification as a *NG* and with a possible star-forming origin of its X-ray luminosity (Pereira-Santaella et al. 2011; Ranalli et al. 2012), as discussed above. Thus, G107 might be either a very weak AGN whose optical/IR emission is diluted by the host galaxy, or a spiral galaxy with intense star formation (see Figure 3 and Table 1 in RA09).

ID	z_{spec}		Comp.	H α		[N II] λ 6584		H β		[O III] λ 4959		[O III] λ 5007	
	z_{opt}	z_{NIR}		Flux	FWHM	Flux	FWHM	Flux	FWHM	Flux	FWHM	Flux	FWHM
17	1.284	1.284	N	1.06 \pm 1.52	820	10.1 \pm 1.9	810	21.2 \pm 2.0	800
			B	55.7 \pm 4.93	3400
25	0.761	0.761	N	1.48 \pm 0.24	\leq 340	1.16 \pm 0.21	\leq 340	[0.25 \pm 0.02]	[140]	[0.07]	[130]	[0.17 \pm 0.02]	[130]
26	0.808	0.808	N	1.03 \pm 0.33	\leq 280	0.72 \pm 0.20	\leq 250	[0.09 \pm 0.02]	[70]	[0.05]	[70]	[0.10 \pm 0.01]	[70]
27	0.683	-	N	:0.60	...	:0.60	...	[0.18 \pm 0.04]	[50]	[0.29 \pm 0.02]	[\leq 80]	[0.89 \pm 0.05]	[\leq 80]
36	0.281	-	N	[0.66 \pm 0.02]	[280]	[0.34 \pm 0.01]	[280]
43	0.532	0.534	N	Abs	720	0.6 \pm 0.3	720	[Abs]	[700]	[0.08]	...	[0.08]	...
45	-	1.268	N	:0.33	\leq 190	0.48 \pm 0.13	\leq 190	Abs	\leq 180	:0.27	\leq 250	0.55 \pm 0.13	\leq 250
47	0.418	0.418	N
53	0.723	0.722	Nb	1.47 \pm 0.11	\leq 340	0.22 \pm 0.09	\leq 340	[0.08 \pm 0.01]	[\leq 75]	[0.06]	[\leq 70]	[0.06]	[\leq 70]
			Nr	[0.13 \pm 0.02]	[\leq 75]	[0.06]	[\leq 70]	[0.10 \pm 0.01]	[\leq 70]
55	1.211	1.212	N	0.5 \pm 0.2	\leq 180	0.27 \pm 0.20	\leq 180	:0.23	...	:0.23	...	:0.23	...
			B	:2.02	1460	:1.65
56	1.208	1.213	N	0.88 \pm 0.24	180	:0.33	180	:0.20	...	:0.20	...	:0.20	...
57	-	0.651	N
59	0.465	0.465	N	1.42 \pm 0.50	230	1.05 \pm 0.47	230	[0.32 \pm 0.02]	[220]	[1.09 \pm 0.03]	[210]	[3.46 \pm 0.04]	[210]
60	0.484	0.484	N	1.14 \pm 1.10	230	1.6 \pm 0.6	230	[0.34 \pm 0.02]	[170]	[0.30 \pm 0.02]	[160]	[1.02 \pm 0.03]	[160]
			B	6.09 \pm 1.66	1510	[0.91 \pm 0.08]	[1530]
62	0.902	0.902	N	2.87 \pm 0.46	50	1.1 \pm 0.4	50	:0.97	40	:0.97	40	1.67 \pm 0.46	40
63	0.482	0.482	Nb	4.82 \pm 0.98	590	4.67 \pm 1.25	590	[0.07 \pm 0.02]	[880]	[0.23 \pm 0.03]	[850]	[0.69 \pm 0.11]	[840]
			Nr	2.39 \pm 0.68	230	1.33 \pm 0.64	230	[0.10 \pm 0.03]	[180]	[0.52 \pm 0.03]	[310]	[1.57 \pm 0.08]	[310]
			B	35.7 \pm 4.0	5530	[12.7 \pm 1.5]	[5880]
73	0.986	-	N	:0.79	...	:0.79	:1.13	...	:1.13	...
74	0.551	0.551	Nb	5.25 \pm 0.53	280	1.29 \pm 0.44	280	[0.53 \pm 0.07]	[120]	[0.40 \pm 0.03]	[65]	[1.2 \pm 0.1]	[65]
			Nr	[0.49 \pm 0.07]	[120]	[0.36 \pm 0.03]	[150]	[1.09 \pm 0.08]	[150]
76	0.271	-	N	[Abs]	[210]	[0.9 \pm 0.2]	[210]
78	0.985	0.986	N	17.97 \pm 0.13	360	3.15 \pm 1.56	410
			B	62.91 \pm 0.34	3180
90	1.148	1.148	N	19.4 \pm 3.2	640	16.4 \pm 4.7	640	2.58 \pm 1.33	780	4.78 \pm 0.67	760	14.3 \pm 0.8	750
			B	52.6 \pm 8.9	1830	12 \pm 2	1820
91	0.873	0.873	N	1.07 \pm 0.27	\leq 260	1.07 \pm 0.25	\leq 260	Abs	360	1.47 \pm 0.38	350	2.61 \pm 0.48	\leq 310
93	0.985	0.987	N	2.44 \pm 0.83	130	3.58 \pm 0.79	130	:0.81	120	:0.81	120	2.05 \pm 0.47	120
99	0.996	0.996	N	:0.61	...	1.1 \pm 0.3
105	-	0.569	N	1.01 \pm 0.35	\leq 370	:0.68	\leq 370
106	-	0.986	N	:1.03	95	:1.03	95
107	0.671	0.670	N	2.6 \pm 0.9	90	1.22 \pm 0.57	90	[0.37 \pm 0.07]	[\leq 90]	[0.37]	[\leq 85]	[0.37]	[\leq 85]
			B	2.05 \pm 1.21	870	[3.12]	[850]
110	-	0.731	N	1.74 \pm 0.47	270	:0.69	270

Table 3. Line fluxes and FWHMs. Columns 2 and 3 list the spectroscopic redshifts from optical and NIR spectra, respectively. Column 4 corresponds to the line component that has been fitted (B: broad, N: narrow, Nb: blueshifted narrow, and Nr: redshifted narrow component). Lines fluxes ($\times 10^{-16}$ erg s $^{-1}$ cm $^{-2}$) and FWHMs (km s $^{-1}$) of H α , [N II] λ 6584, H β , and [O III] λ 4959, 5007 are reported. The line flux errors reported are given by DIPSO, and they include the uncertainty associated to the fit. For several faint/undetected transitions, the continuum noise was used to calculate a 1.5 σ upper limit to the line emission (those starting with :). For the sources lacking a secure spectroscopic redshift (G45, G57, G105, G106 and G110), a larger detection significance of 2 σ is required. Brackets indicate that measurements are from DEEP2 optical spectra. Line widths have been corrected from instrumental broadening (18 and 3.6 Å for the LIRIS and DEEP2 spectra respectively). Typical line width uncertainties are 25–30%.

Similar positions, also in the composite region, are occupied by the two *SB-dom* G26 and G62 and the *NGs* G25 and G74, confirming their SED classifications. Attending to their X-ray luminosities, only the galaxy G62 ($L_X \leq 42.55$ erg s $^{-1}$) could not be an AGN.

The position of the sources G53 and G59 in the BPT diagram is noticeable. We classified G53 as a *Type-2*, and its $L_X > L_X^{AGN}$, but it is well below the H II boundary in the more restrictive Kewley et al. (2001) definition. This source is likely a weak AGN with intense star formation. On the other hand, G59, whose SED was fitted with a spiral template in RA09 and has $L_X < L_X^{AGN}$, appears in the AGN region of the diagram, very close to the quasar G63. Thus, the galaxy G59 is likely a heavily obscured Type-2 AGN. In summary, according to the emission line fluxes represented in Figure 11, our SED classification is correct for 9/11 galaxies.

Our previous work was aimed to distinguish between pure and host galaxy-dominated AGNs using SED fitting

over a broad wavelength range. The use of accurate multi-wavelength photometry, which is now available for several deep fields, to classify AGN, instead of spectroscopy, represents huge savings of both telescope time and data reduction effort. From the comparison presented here, we find that the SED classification method employed in RA09 works for 89% of a representative sample of X-ray and MIR sources at $z \sim 0.8$ (see Table 5).

To further investigate the level of AGN-dominance in these galaxies, in Figure 12 we compare their observed hard X-ray fluxes (Waskett et al. 2004; Nandra et al. 2005) and 24 μ m fluxes (Barmby et al. 2006) as in Alonso-Herrero et al. (2004). The area between dotted lines corresponds to the extrapolation of the median hard X-ray-to-MIR ratios ($\pm 1\sigma$) of local AGN ($z < 0.12$) selected in hard X-rays by Piccinotti et al. (1982). Same but for local starburst galaxies from Ranalli et al. (2003) is the region between dashed lines. The plot looks very similar to Figure 1 in Alonso-Herrero et al. (2004), where galaxies with red-

ID	z_{spec}	Comp.	H α broad		Group	Agreement	AGN
			FWHM (km s $^{-1}$)	Log L (erg s $^{-1}$)			
17	1.284	N, B	3400 (H β)	43.69 (H β)	Type-1	✓	✓
25	0.761	N	NG	✓	✓
26	0.808	N	SB-dom	✓	✓
27	0.683	N	SB-cont	✓	✓
36	0.281	N	NG	✓	✓
43	0.532	N	NG	✓	✓
45	1.268	N	SB-dom	✓	✓
47	0.418	N	NG	✓	?
53	0.723	Nb, Nr	Type-2	X	✓
55	1.212	Nb, Nr, B	1500	≤ 42.19	SB-dom	✓	?
56	1.208	N	Type-2	✓	✓
57	0.651	N	Type-2	✓	✓
59	0.465	N	NG	X	✓
60	0.484	N, B	1500	41.68	Type-2	X	✓
62	0.902	Nb, Nr	SB-dom	✓	?
63	0.482	Nb, Nr, B	5500	42.45	Type-1	✓	✓
73	0.986	N	NG	✓	✓
74	0.551	Nb, Nr	NG	✓	✓
76	0.271	N	NG	✓	✓
78	0.986	N, B	3200	43.46	Type-1	✓	✓
90	1.148	N, B	1800	43.55	SB-cont	✓	✓
91	0.873	N	SB-dom	✓	✓
93	0.987	N	Type-2	✓	✓
99	0.996	Nb, Nr	NG	✓	✓
105	0.569	N	Type-2	✓	✓
106	0.986	N	Type-2	✓	✓
107	0.670	N, B	900	41.55	NG	✓	?
110	0.731	N	Type-2	✓	✓

Table 5. Comparison between spectroscopic data and SED fitting. Column 2 corresponds to z_{spec} measured from the NIR and optical lines (see Table 3). In case of disagreement, we chose the most reliable value in terms of the S/N of the lines identified in each case. Columns 3, 4, and 5 indicate the emission line components fitted (B: broad, N: narrow, Nb: blueshifted narrow, and Nr: redshifted narrow component) and the FWHM and luminosity of the broad component of H α (H β in the case of G17), if present. Column 6 lists the SED-based classification of the galaxies as in RA09. Finally, columns 7 and 8 indicate whether or not there is agreement between the spectral and SED classifications, and if the presence of nuclear activity has been confirmed from the different diagnostic diagrams employed here.

shifts in the range $z=0.2-1.6$ were represented. Some of the AGN occupy the local AGN region and the rest lie in the transition zone between local starbursts and AGN. Of the 28 objects in Figure 12, 18 are lying below the local AGN region ($\sim 64\%$), indicating either high absorption in the X-rays or intense star formation contributing to the 24 μm emission. Considering the relatively low values of the hydrogen column densities reported in Table 6 from Georgakakis et al. (2006), the first possibility is unlikely. We note, however, that the overall majority of the galaxies are very close to the local AGN region.

The position of the galaxies G17 and G90 in Figure 12 is remarkable. They are the brightest 24 μm sources in the whole sample studied in Barmby et al. (2006)⁹ and despite their strong H β and H α broad components, they lie well below the AGN area of the diagram, indicating a strong contribution from star-heated dust at 24 μm .

It is also worth mentioning the position of the galaxies G53 and G59 in Figure 12. Whereas G59 lies in the AGN

⁹ 13.72 \pm 0.01 and 14.51 \pm 0.01 mag at 24 μm for G17 and G90 respectively.

region of the BPT diagram shown in Figure 11, in Figure 12 appears considerably shifted from the local AGN region. Considering its low hydrogen column density ($N_H < 0.58 \times 10^{22} \text{ cm}^{-2}$; Georgakakis et al. 2006), the classification of this galaxy is unclear, although the BPT diagram confirms the presence of an active nucleus. Exactly the opposite happens to G53, which is definitely in the H II region of the BPT, but has typical MIR and hard X-ray AGN fluxes. In Table 5 we considered G53 and G59 as failures in the SED classification, but according to Figure 12, it appears to be correct.

Summarising, in view of all the discussed diagnostic diagrams, X-ray luminosities and SED classification, we cannot confirm the presence of nuclear activity in 4/28 sources (14% of the sample): G47, G55, G62 and G107. These galaxies 1) have $L_X < L_X^{AGN}$, 2) SEDs fitted with galaxy or starburst templates and 3) lie outside the AGN region in Figures 11 and 12. Note that they are the only four galaxies in the sample with upper limits for their X-ray luminosities (see Table 1). They could be low-luminosity AGN heavily obscured in the X-rays, but we cannot confirm it. Thus, in the following, we will exclude these four galaxies from the re-

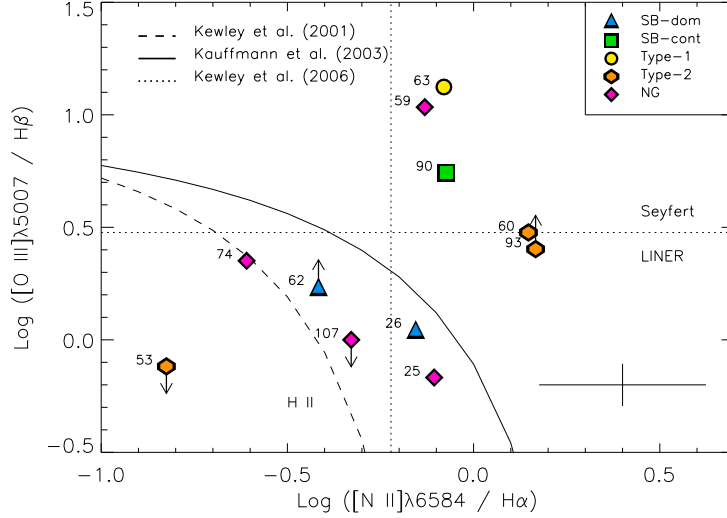


Figure 11. BPT diagram involving the emission-line flux ratios $[OIII]/H\beta$ and $[NII]/H\alpha$ for the 11 galaxies in our sample with detections of the four emission lines involved. The empirical separations between AGN and H II regions, as defined in Kewley et al. (2001) and Kauffmann et al. (2003), are shown together with the boundaries between LINERs and Seyfert galaxies ($[OIII]/H\beta=3$ and $[NII]/H\alpha=0.6$). The error bars at the bottom right corner correspond to the typical uncertainties of the two ratios.

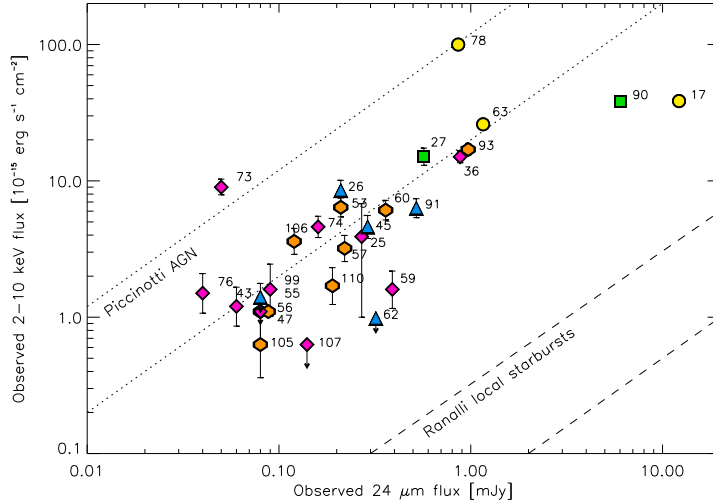


Figure 12. Observed 24 μm versus 2-10 keV fluxes. The areas between dotted and dashed lines correspond to the AGN region defined in Alonso-Herrero et al. (2004) from the Piccinotti et al. (1982) X-ray-selected AGN sample and to the local starburst region as defined in Ranalli et al. (2003) respectively. Symbols are the same as in Figure 11. 24 μm flux errors are smaller than symbols (representative error is 0.01 mJy).

sults found for AGN, although, for simplicity, we will refer to the whole sample of 28 galaxies as “the AGN sample”.

4.2 SFR from $H\alpha$ luminosity

By putting together the optical and NIR spectra of the galaxies, we have emission line flux measurements of $H\alpha$ for 18/28 galaxies and upper limits for another five (see Table 3). In Table 6 we report the observed $H\alpha$ luminosities ($L_{H\alpha}$) obtained using the corresponding luminosity distances. In the absence of an AGN, the $H\alpha$ luminosity is the best indicator of the instantaneous SFR, since $H\alpha$ has little dependence

on metallicity and it is much less affected by dust attenuation than the rest-frame UV continuum and $Ly\alpha$ (Kennicutt 1998; Bicker & Fritze-v. Alvensleben 2005).

In order to obtain SFRs for the galaxies in the sample using their $H\alpha$ luminosities, we have to correct $L_{H\alpha}$ from attenuation, using the A_V values reported in Table 6. We calculated them using the $H\alpha$ and $H\beta$ narrow-line fluxes, when available, and the standard Galactic extinction curve of Cardelli et al. (1989) with $R_V=3.1$:

$$A_V(\text{mag}) = 3.1 \times E(B - V) = 6.169 \times [\text{Log}(H\alpha/H\beta) -$$

ID	Comp.	Line	Flux	FWHM
36	N	[S II] λ 6732	[0.17 \pm 0.01]	[260]
43	N	[O II] λ 7320	0.31 \pm 0.17	530
45	N	H γ	Abs	150
	N	[O III] λ 4363	0.34 \pm 0.10	\leq 280
47	N	[O II] λ 7320	0.46 \pm 0.14	220
53	N	[S II] λ 6732	0.31 \pm 0.30	\leq 340
55	Nb	[O II] λ 3727	[0.09 \pm 0.01]	[95]
	Nr		[0.10 \pm 0.02]	[95]
56	N	[O II] λ 3727	[0.17 \pm 0.03]	[170]
57	N	[O II] λ 7320	2.79 \pm 0.24	180
59	N	[O II] λ 7320	1.28 \pm 0.40	210
62	Nb	[O II] λ 3727	[0.24 \pm 0.11]	[130]
	Nr		[0.50 \pm 0.12]	[160]
63	N	[O I] λ 6300	2.09 \pm 0.97	470
74	N	[S II] λ 6732	0.86 \pm 0.32	270
90	N	[O II] λ 3727	[1.63 \pm 0.10]	[490]
91	N	[O II] λ 3727	[0.59 \pm 0.05]	[320]
93	Nb	[O II] λ 3727	[0.14 \pm 0.20]	[240]
	Nr		[0.51 \pm 0.20]	[320]
99	N	[O II] λ 7320	1.24 \pm 0.54	170
	N	[S II] λ 6732	:0.61	170
	Nb	[O II] λ 3727	[0.2 \pm 0.03]	[120]
	Nr		[0.2 \pm 0.04]	[120]
110	N	[O I] λ 6300	0.72 \pm 0.41	280

Table 4. Same as in Table 3, but for other lines detected in the LIRIS and/or DEEP2 spectra.

0.486]

Then, we obtained reddening values at the wavelength of emission of H α ($A_{H\alpha}$), and we used them to correct $L_{H\alpha}$ from extinction. In Table 6 we report the attenuation-corrected H α luminosities ($L_{H\alpha}^{corr}$) and corresponding errors.

The H α emission in non-active galaxies is produced almost entirely by massive stars ($M > 10M_{\odot}$), but in active galaxies it includes a contribution from gas photoionised by the AGN. In fact, this contribution will dominate in the case of pure AGN, and it will be, in principle, less important in the case of buried AGN. To test the latter, in Figure 13 we represent $L_{H\alpha}$ versus $L_{2-10keV}$ from Waskett et al. (2004) and Nandra et al. (2005). Those X-ray luminosities are not absorption-corrected, but considering the relatively low values of the hydrogen column densities reported in Table 6 from Georgakakis et al. (2006), we assume that they are not going to differ significantly from the intrinsic hard X-ray luminosities. The H α luminosities plotted in Figure 13 are not extinction-corrected either, because we only have attenuation-corrected values for half of the sample (see Table 6).

If we consider the 2-10 keV luminosity as a proxy of the AGN, it should be correlated with $L_{H\alpha}$ for AGN-dominated objects. Thus, we can derive an empirical relationship between $L_{H\alpha}$ and L_X using the four galaxies that we can definitely classify as AGN-dominated from their spectra, SED fits, and diagnostic diagrams presented in this work: G60, G63, G78, and G93. By fitting them, we find a correlation in the form $\text{Log}(L_{H\alpha}^{AGN}) = 0.95 \text{Log}(L_X) + 0.39$, with a correlation coefficient $r=0.99$. G60 has a larger error bar than the other three pure-AGN (see Figure 13) because of the multi-

component fit performed to derive the H α flux, in addition to its lower H α emission as compared to that of G63, G78, and G93. However, in spite of its large error bar, G60 should be included in the AGN fit because it is the only pure-AGN representative of the lower luminosity objects in the sample. To ensure that we are not introducing any bias in the determination of $L_{H\alpha}^{AGN}$ by including G60, we performed the test of excluding it from the AGN fit, and we found $\text{Log}(L_{H\alpha}^{AGN}) = 0.87 \text{Log}(L_X) + 3.80$, with $r=0.98$. The differences between the $L_{H\alpha}^{AGN}$ values derived from the two fits are much smaller than the $L_{H\alpha}^{SF}$ errors quoted in Table 6. Therefore, we can include G60 in the fit without introducing any bias in the final results.

Of the four pure-AGN, G93 is the only one whose H α flux could be marginally affected by sky line contamination. Looking carefully at the exact position of the sky lines, none of them coincides with $\lambda(H\alpha)$, but the residuals of the sky subtraction could marginally affect the blue wing of H α . To test how this could affect the determination of $L_{H\alpha}^{AGN}$, we repeated the same exercise as for G60, but excluding G93. In this case we obtained $\text{Log}(L_{H\alpha}^{AGN}) = 0.97 \text{Log}(L_X) - 0.40$, with $r=0.99$, which is even more similar to the original fit than when we excluded G60. Thus, including G93 makes no significant difference to $L_{H\alpha}^{AGN}$, and ultimately, to $L_{H\alpha}^{SF}$.

The luminosity of H α will be partly due to the AGN and to the star formation ($L_{H\alpha} = L_{H\alpha}^{AGN} + L_{H\alpha}^{SF}$). If the 2-10 keV luminosity probes the AGN, objects lying above the correlation will have a significant contribution from star formation in their H α emission (e.g. G56, G59, G62, G74, G105, G107 and G110). These galaxies have relatively low hard X-ray luminosities, indicating the presence of either a weak/absent AGN with intense star formation or a heavily obscured AGN. At the high luminosity end, the *SB-cont* G90 shows an excess of H α emission as well, explaining its position in Figure 12. On the other hand, we have two galaxies lying below the correlation (e.g. G27 and G36). In the case of G36, high attenuation could be affecting its H α emission, whereas in the case of G27 ($A_V \leq 0.23$ mag) its H α flux could be compromised by the line position, close to the edge of the detector (see Figure 4).

Galaxies lying close to the AGN correlation shown in Figure 13 will have $L_{H\alpha} \approx L_{H\alpha}^{AGN}$, whereas for those located well above, the $L_{H\alpha}^{SF}$ contribution to H α will be significant. Thus, we use our AGN empirical correlation to calculate, for a given L_X , the expected $L_{H\alpha}^{AGN}$ of the galaxies. We then subtract this AGN contribution from the attenuation-corrected $L_{H\alpha}^{corr}$ values to obtain $L_{H\alpha}^{SF}$ (see Table 6). For the galaxies well below the correlation ($L_{H\alpha} << L_{H\alpha}^{AGN}$) we cannot estimate the AGN contribution to H α even when $L_{H\alpha}$ has been extinction-corrected, and thus we have used the total $L_{H\alpha}$ values as upper limits.

Ideally, this evaluation of the AGN contribution should have been done using attenuation-corrected H α luminosities and intrinsic hard X-ray fluxes, since reddening in the optical and in the X-rays can be different (Fiore et al. 2012). However, we only have A_V values for 9 galaxies and upper limits for another two. Besides, out of the four AGN-dominated sources that we use to derive the AGN correlation, only G60 has a reliable extinction value¹⁰. On the other hand,

¹⁰ We have likely overestimated the A_V value for G63 ($A_V=7\pm 2$)

ID	Dist (Mpc)	A_V (mag)	$L_{H\alpha} \times 10^{41}$ (erg s $^{-1}$)	$L_{H\alpha}^{corr} \times 10^{41}$ (erg s $^{-1}$)	$L_{H\alpha}^{SF} \times 10^{41}$ (erg s $^{-1}$)	SFR ($L_{H\alpha}^{SF}$) (M_{\odot} yr $^{-1}$)	F_{24}^{obs} (mJy)	SFR (F_{24}^{SF}) (M_{\odot} yr $^{-1}$)	$L_X \times 10^{43}$ (erg s $^{-1}$)	$N_H \times 10^{22}$ (cm $^{-2}$)	Group
17	8597	12.19±0.11 (74%)	>1000	33.9±2.5	...	3
25	4481	1.77±1.11	3.55±0.58	13.3±11.3	11.4±11.3	6±6	0.27±0.01 (69%)	8	0.93±0.69	...	5
26	4823	3.53±2.40	2.86±0.92	40.0±72.9	35.4±72.9	19±40	0.21±0.01 (35%)	17	2.35±0.44	...	1
27	3916	≤0.23	≤1.10	≤1.10	≤1.10	≤0.6	0.57±0.01 (85%)	6	2.77±0.40	...	2
36	1358	...	0.15±0.01	≥0.15	0.88±0.01 (36%)	4	0.33±0.03	8.82	5
43	2885	0.06±0.01 (0%)	2	0.12±0.04	3.36	5
45	8449	...	≤2.82	0.29±0.01 (5%)	1000	3.91±0.76	<0.08	1
47	2159	0.08±0.01 (7%)	1	≤0.06	<0.08	5
53	4203	2.21±0.99	3.11±0.23	16.2±12.0	13.4±12.0	7±7	0.21±0.01 (72%)	4	1.35±0.22	5.51	4
55	7990	...	3.82±1.53	≥3.82	≥1.63	≥1	0.08±0.01 (4%)	77	≤1.06	<2.15	1
56	7963	≥0.97	6.67±1.82	≥13.8	≥12.0	≥7	0.08±0.01 (82%)	4	0.83±0.42	0.53	4
57	3681	0.22±0.01 (51%)	7	0.52±0.11	0.33	4
59	2451	0.99±2.21	1.02±0.36	2.14±3.61	1.88±3.61	1±2	0.39±0.01 (81%)	2	0.11±0.04	<0.58	5
60	2571	0.24±5.96	0.90±0.87	1.08±4.91	0.05±4.92	0.03±2.71	0.36±0.01 (41%)	7	0.48±0.08	<0.24	4
62	5528	...	10.5±1.7	≥10.5	≥9.72	≥5	0.32±0.01 (0%)	94	≤0.36	<5.84	1
63	2558	7.04±2.30	5.64±1.30	1084±1880	1080±1880	595±1034	1.16±0.01 (100%)	...	2.02±0.15	<0.12	3
73	6179	...	≤3.61	0.05±0.01 (0%)	9	4.09±0.55	0.72	5
74	3009	1.39±1.05	5.68±0.57	16.1±12.7	15.0±12.7	8±7	0.16±0.01 (25%)	5	0.50±0.09	2.16	5
76	1303	0.04±0.01 (23%)	0.1	0.03±0.01	0.02	5
78	6171	...	81.8±0.6	≥81.8	≥4.12	≥2	0.86±0.01 (97%)	3	45.3±1.7	<0.04	3
90	7474	2.41±3.34	130±21	784±1961	740±1961	407±1079	6.02±0.05 (91%)	>1000	25.3±1.6	1.16	2
91	5307	...	3.60±0.91	≥3.60	0.52±0.01 (0%)	163	2.11±0.34	20.77	1
93	6173	...	11.1±3.8	≥11.1	0.97±0.01 (65%)	166	7.71±0.73	3.89	4
99	6262	...	≤2.86	0.09±0.01 (20%)	17	0.75±0.33	3.63	5
105	3123	...	1.18±0.41	≥1.18	≥1.01	≥0.6	0.08±0.01 (69%)	1	0.07±0.04	2.25	4
106	6179	...	≤4.70	0.12±0.01 (74%)	4	1.64±0.36	20.46	4
107	3830	2.22±2.43	4.56±1.58	23.9±44.2	≥23.7	≥13	0.14±0.01 (30%)	7	≤0.11	<2.12	5
110	4250	...	3.76±1.01	≥3.76	≥2.97	≥2	0.19±0.01 (96%)	0.2	0.37±0.11	<0.26	4

Table 6. Observed, attenuation-corrected, and AGN-corrected $H\alpha$ luminosities calculated using the fluxes reported in Table 3 and the luminosity distances listed in column 2. The optical extinction listed in column 3 has been obtained from the observed $H\alpha/H\beta$ ratios when available. Column 7 lists the SFRs obtained from $L_{H\alpha}^{SF}$. Column 8 corresponds to the observed 24 μ m fluxes and the percentage of AGN contamination removed from the latter to calculate the IR SFRs reported in column 9, which have an accuracy of better than 0.2 dex; (Rieke et al. 2009). Columns 10, 11, and 12 indicate the 2-10 keV X-ray luminosities from Nandra et al. (2005) and Waskett et al. (2004), the column densities from Georgakakis et al. (2006), and the SED classification as in Table 1.

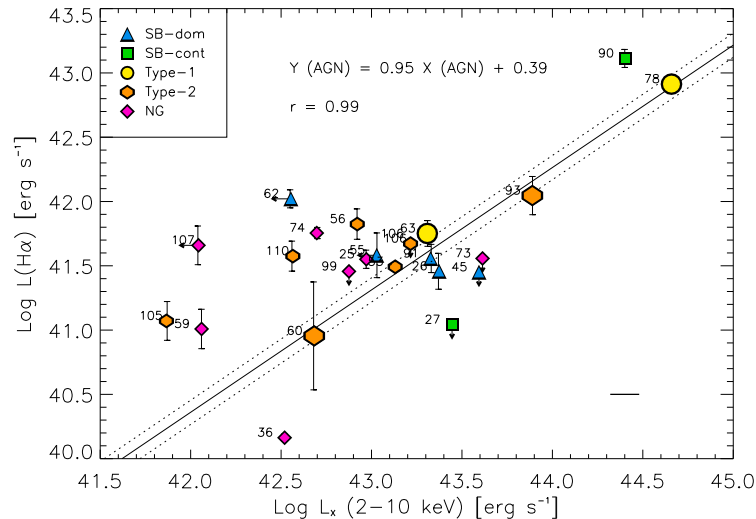


Figure 13. $H\alpha$ versus hard X-ray luminosity (2-10 keV). Solid and dotted lines correspond to the AGN empirical relationship determined using the four AGN-dominated galaxies G60, G63, G78, and G93 (plotted with larger symbols) and 1σ limits, respectively. The correlation coefficient is $r=0.99$. Objects well above this line are likely dominated by star formation, whereas those below may have $H\alpha$ fluxes affected by extinction. L_X representative error is represented at the bottom right corner.

the observed and intrinsic hard X-ray luminosities will be similar, considering the low N_H values (Georgakakis et al. 2006). Thus, our method will be more reliable for galaxies with similar levels of obscuration in the optical and in the X-rays and vice versa.

We can now estimate SFRs for the galaxies in our sample using our individual $L_{H\alpha}^{SF}$ values and the Kennicutt (1998) conversion for Case B recombination at $T_e=10,000$ K (Osterbrock 1989), assuming solar metallicity and a Kroupa & Weidner (2003) initial mass function (IMF):

$$\text{SFR} (M_{\odot} \text{ yr}^{-1}) = 5.5 \times 10^{-42} L_{H\alpha}^{SF} (\text{erg s}^{-1})$$

We obtain $\text{SFR}(L_{H\alpha}^{SF}) = [0.03, 19] M_{\odot} \text{ yr}^{-1}$, and two extreme values of 407 and 595 (± 1000) $M_{\odot} \text{ yr}^{-1}$ for the *Type-1s* G63 and G90 respectively. In the case of G63, it is likely that we have overestimated the extinction ($A_V=7\pm 2$ mag), because the fit of the $H\beta$ profile using multiple components was particularly challenging. This galaxy does not appear to have such an intense star formation in Figure 12, as opposed to G90. We will discuss the case of these two galaxies in Section 4.3.

The individual SFRs, with the exception of those of G63 and G90, are among the lowest reported in the literature for samples of non-active star-forming galaxies at similar redshifts and stellar masses (e.g. Twite et al. 2012 and Rodríguez-Eugenio et al. in prep.), as we discuss in Section 5.

The average and median SFRs, measured using the values reported in Table 6, including upper and lower limits as fixed values, are 5 ± 5 and $2 M_{\odot} \text{ yr}^{-1}$. We have excluded the extreme SFRs of G63 and G90 because of their large uncertainties, and those of G55, G62 and G107 because they are not confirmed AGN.

If we do not consider the upper and lower limits (i.e., if we only use the SFRs of the galaxies G25, G26, G53, G59, G60 and G74) the average and median SFRs are 7 ± 7 and $7 M_{\odot} \text{ yr}^{-1}$. Note that none of these six galaxies has its $H\alpha$ emission affected by sky line contamination.

4.3 SFR from observed 24 μm emission

In dusty galaxies, the UV light emitted by young stars is absorbed by dust and re-emitted in the IR. Therefore, the IR luminosity, either monochromatic or total, can be used to estimate the SFR (Kennicutt et al. 2009). In particular, the 24 μm luminosity is a good indicator of the current SFR of dusty star-forming galaxies (e.g. Alonso-Herrero et al. 2006; Calzetti et al. 2007; Rieke et al. 2009).

For galaxies whose $H\alpha$ emission is obscured, both the AGN- and star-heated dust should be detected in the MIR. Thus, by comparing the $H\alpha$ and 24 μm luminosities we can distinguish between galaxies with apparently low SFRs due to high levels of extinction and galaxies with negligible star formation. In Figure 14 we compare the individual values of $L_{H\alpha}/L_X$ and L_{24}/L_X . The horizontal lines represent the mean AGN ratio in each case, using the four pure-AGN G60, G63, G78, and G93. The galaxies G56, G59, G90, G105, G107, and G110 are well above the mean AGN ratios, indicating a strong contribution of star formation.

mag). The fitting of its $H\beta$ profile using multiple components was particularly difficult.

On the contrary, the *NG* G74, which in the left panel of Figure 14 is clearly above the AGN mean $L_{H\alpha}/L_X$, has a low L_{24}/L_X ratio. As discussed in Kennicutt et al. (2009), the galaxies with relatively low $H\alpha$ luminosities ($L(H\alpha) < 10^{42}$ erg s $^{-1}$) tend to have little dust, and consequently low A_V and weak IR emission. This could be the case of the galaxies G53 and G74.

The four galaxies for which we cannot confirm the presence of nuclear activity, G47, G55, G62 and G107, show large L_{24}/L_X values, indicative of warm dust emission produced by intense star formation and/or a heavily obscured AGN. The position of the galaxies G63 and G90 in the two panels of Figure 14 confirms what we discussed in Section 4.2. G63 does not have a large L_{24}/L_X value as it is the case for G90. Thus, the extreme SFR measured from its $H\alpha$ luminosity is likely the result of an overestimation of the A_V , whereas in the case of G90 it is probably real, although affected by a large uncertainty. In addition, G90 has its $H\alpha$ emission somehow affected by sky line contamination.

The largest L_{24}/L_X value corresponds to the *Type-1* G17, for which we do not have an $H\alpha$ measurement due to the galaxy redshift ($z=1.28$). Finally, the *SB-dom* G45 and G91 show a MIR excess as compared to the $H\alpha$ emission, indicative of relatively large A_V and in agreement with their SED classification as *SB-dom*.

To estimate SFRs using observed 24 μm emission, it is necessary to remove the contribution of AGN-heated dust from the total MIR emission, as we did for the $H\alpha$ luminosities.

We have estimated the AGN contribution to the 24 μm emission of the individual galaxies using the SED fits shown in Figure 2. For *Type-1* and *Type-2*, we have subtracted the 24 μm flux of the fitted template from the observed 24 μm flux. We assume that the flux difference corresponds to dust heated by star formation. The median AGN contributions are 97% in the case of *Type-1* and 72% for *Type-2* (see column 8 in Table 6). For the galaxies classified as *SB-dom* and *NG*, we consider that the 24 μm fluxes of the fitted templates are representative of the star formation, and any excess in the observed fluxes is due to the AGN (median AGN contribution of 4% in the case of *SB-dom* and 25% for *NG*). Finally, for the two *SB-cont*, we have repeated the SED fits using a *Type-2* template in the case of G27, and a *Type-1* template for G90, and consider the difference between the fitted and observed 24 μm fluxes as due to star-heated dust. The AGN contributions are 85% for G27 and 91% for G90.

We could have corrected the 24 μm fluxes from AGN contamination using the same technique employed in Section 4.2, but then we would have been left with no correction for those galaxies lying below the AGN mean ratio in Figure 14.

Using the AGN-corrected 24 μm fluxes F_{24}^{SF} and equation 14 in Rieke et al. (2009):

$$\text{Log SFR} (M_{\odot} \text{ yr}^{-1}) = A(z) + B(z)[\text{Log}(4\pi D_L^2 F_{24}^{SF}) - 53],$$

we can calculate IR SFRs for the 28 galaxies in our sample (see Table 6). $A(z)$ and $B(z)$ are the SFR fit coefficients as a function of redshift for MIPS, and the above calibration assumes the Kroupa & Weidner (2003) IMF. We obtain values of $\text{SFR} (F_{24}^{SF}) = [0.1, 166] M_{\odot} \text{ yr}^{-1}$ and three extreme values of $\gtrsim 1000 M_{\odot} \text{ yr}^{-1}$ for the galaxies G17, G45, and G90. SFRs larger than $1000 M_{\odot} \text{ yr}^{-1}$ are only measured in

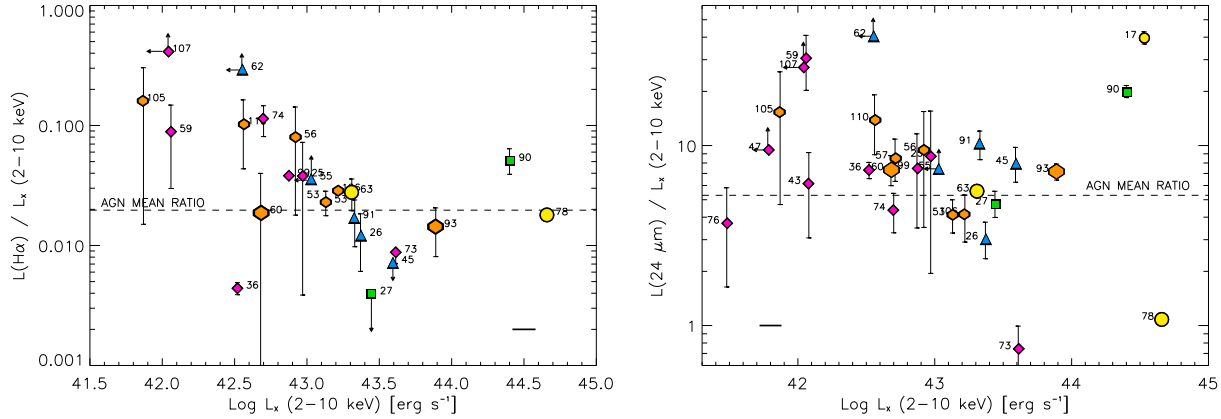


Figure 14. Left: $L_{H\alpha}/L_X$ versus hard X-ray luminosity (2-10 keV). Objects with a significant contribution of $H\alpha$ due to star formation are clearly offset from the locus of galaxies. The horizontal dashed line corresponds to the mean value of $L_{H\alpha}/L_X$, considering the four pure AGN G60, G63, G78, and G93. Right: same as in the left panel, but for L_{24}/L_X . L_X representative error is represented at the bottom of the two panels.

ULIRGs and/or extreme starbursts (Magnelli et al. 2010). Given the position of G17 and G90 in Figure 12 and in the right panel of Figure 14, the two galaxies must be ULIRGs. In fact, they both have monochromatic $24\ \mu\text{m}$ luminosities larger than $45.5\ \text{erg s}^{-1}$, exclusive of this type of object (Alonso-Herrero 2007). The case of G45 is different. In the right panel of Figure 14 the galaxy does not show a strong excess in $24\ \mu\text{m}$ over the AGN mean ratio. This indicates that we may have underestimated its AGN contribution to the $24\ \mu\text{m}$ flux (only 5%).

In general we find $\text{SFR}(F_{24}^{SF}) \gtrsim \text{SFR}(L_{H\alpha}^{SF})$, although for some galaxies $\text{SFR}(F_{24}^{SF}) < \text{SFR}(L_{H\alpha}^{SF})$. This is expected, since the relation between $H\alpha$ and $24\ \mu\text{m}$ is non-linear, even when the $H\alpha$ emission has been corrected from attenuation (see Figure 6 in Kennicutt et al. 2009). The average and median SFRs that we obtain from the $24\ \mu\text{m}$ fluxes are 20 ± 50 and $5\ M_{\odot}\ \text{yr}^{-1}$ respectively. We have excluded the extreme values of G17, G90 and G45 –which we do not consider representative of the sample– and those of the non-confirmed AGN. The median SFR is in agreement with that derived from the attenuation-corrected $H\alpha$ luminosities. This similarity between the $H\alpha$ and $24\ \mu\text{m}$ median SFRs gives us extra-confidence in the AGN corrections that we have employed here.

5 COMPARISON WITH SAMPLES OF NON-ACTIVE GALAXIES

In Sections 4.2 and 4.3 we have estimated SFRs from attenuation- and AGN-corrected $H\alpha$ luminosities and from AGN-corrected $24\ \mu\text{m}$ fluxes. We obtain average SFRs = 7 ± 7 and $20 \pm 50\ M_{\odot}\ \text{yr}^{-1}$ respectively (median SFRs = 7 and $5\ M_{\odot}\ \text{yr}^{-1}$). We now compare our SFRs with those published in the literature for different samples of non-active galaxies of similar stellar masses and redshifts, once converted to the Kroupa & Weidner (2003) IMF. The results of this comparison, including the conversion factors, when necessary, are summarised in Table 7. Although we do not know the individual stellar masses of our galaxies, the sample is representative of the X-ray selected population of

AGN at $z \sim 0.8$, as we showed in Section 2, which typically have stellar masses in the range $0.8\text{--}1.2 \times 10^{11}\ M_{\odot}$ (e.g. Alonso-Herrero et al. 2008).

We first compare with the small sample of 7 star-forming galaxies selected by Doherty et al. (2004) from the Cohen et al. (2000) magnitude-limited sample ($R < 23\ \text{mag}$) at $z \sim 0.8$. We used the $H\alpha$ fluxes and reddening values reported in Tables 1 and 2 in Doherty et al. (2004) to calculate attenuation-corrected SFRs exactly as we did for our AGN. We obtained $\text{SFRs} = [4, 11]\ M_{\odot}\ \text{yr}^{-1}$ for the individual galaxies, and a mean of $7 \pm 3\ M_{\odot}\ \text{yr}^{-1}$, which is very similar to ours. Unfortunately, Doherty et al. (2004) did not give an indication of the stellar masses of their sample.

Secondly, Rodríguez-Eugenio et al. (in preparation) observed a sample of 30 star forming galaxies at $z \sim 1$ and with $M_{*} \sim 10^{10.8}\ M_{\odot}$ in the EGS with LIRIS MOS, for which there are DEEP2 optical spectra as well. They find an average SFR from aperture- and attenuation-corrected $H\alpha$ luminosities of $23 \pm 17\ M_{\odot}\ \text{yr}^{-1}$, with individual values ranging from 5 to $64\ M_{\odot}\ \text{yr}^{-1}$.

Twite et al. (2012) also used LIRIS MOS observations of galaxies at $z \sim 1$ and find attenuation-corrected values of the $\text{SFR} = [4, 319]\ M_{\odot}\ \text{yr}^{-1}$, with an average SFR of $66 \pm 83\ M_{\odot}\ \text{yr}^{-1}$ for the 14 massive galaxies ($M_{*} > 10^{10.5}\ M_{\odot}$) with extinction-corrected $H\alpha$ measurements at the 1.5σ detection level.

Finally, based on $H\alpha$ imaging of a sample of 153 star-forming galaxies at $z \sim 0.8$ with typical stellar masses of $\sim 10^{10}\ M_{\odot}$, Villar et al. (2011) determined attenuation-corrected SFRs = $[3, 23]\ M_{\odot}\ \text{yr}^{-1}$, with a median value of $8\ M_{\odot}\ \text{yr}^{-1}$. This median SFR is very similar to ours (see Table 7). However, the average stellar mass of the Villar et al. (2011) sample is $\sim 10^{10}\ M_{\odot}$, whereas the typical mass of AGN at $z \sim 0.8$ is $\sim 10^{11}\ M_{\odot}$ (Alonso-Herrero et al. 2008). As represented in Figure 14 in Villar et al. (2011), the more massive the galaxies, the larger the SFRs (Dutton et al. 2010; Villar et al. 2011). Thus, it is expected that the galaxies studied in Villar et al. (2011) have lower SFRs than those studied by Twite et al. (2012) and Rodríguez-Eugenio et al. (in preparation).

Again, in spite of the reduced size of the samples com-

Work	Redshift	M_* (M_\odot)	SFRs	Average SFR	Median SFR	IMF factor
Doherty et al. (2004)	~ 0.8	...	[4, 11]	7 ± 3	6	...
Rodríguez-Eugenio et al.	~ 1	$10^{10.8}$	[5, 64]	23 ± 17	19	0.696 (a)
Twite et al. (2012)	~ 1	$> 10^{10.5}$	[4, 319]	66 ± 83	54	1.196 (b)
Villar et al. (2011)	~ 0.8	10^{10}	[3, 23]	...	8	0.696 (a)
This work	~ 0.8	$\sim 10^{11}$	[0.03, 19]	7 ± 7	7	...

Table 7. Comparison with SFRs (from H α) of non-active star-forming galaxies from the literature. Columns 2 and 3 list the average/median redshift and an estimation of the stellar mass of the samples considered. In the case of our AGN sample, we considered a stellar mass of $\sim 10^{11} M_\odot$, typical of AGN at this redshift (Alonso-Herrero et al. 2008). Columns 4, 5, and 6 give the intervals, average (\pm **standard deviation**), and median SFRs of the different samples, once converted to the Kroupa & Weidner (2003) IMF. Finally, column 7 lists the conversion factor applied to convert the SFRs to the Kroupa & Weidner (2003) IMF. Refs: (a) Salpeter (1955); (b) Chabrier (2003).

pared here, as well as the uncertainty affecting our AGN-corrected SFRs, the comparison presented might indicate that the presence of an AGN in a galaxy of $M_* \sim 10^{11} M_\odot$ at $z \sim 0.8$, would be quenching its star formation. This quenching would be reducing the SFR from $20\text{--}50 M_\odot \text{ yr}^{-1}$ (typically found for samples of non-active star-forming galaxies at this redshift and stellar mass: Noeske et al. 2007; Twite et al. 2012; Rodríguez-Eugenio et al. in prep.) to less than $10 M_\odot \text{ yr}^{-1}$. Alternatively, we might be seeing a delay between the offset of the star formation and AGN activity, as observed in the local universe (Davies et al. 2007; Wild et al. 2010).

6 COMPARISON WITH OTHER SAMPLES OF ACTIVE GALAXIES

Star formation activity in the hosts of AGN at intermediate redshift have been studied at longer wavelengths than those analysed here. For example, in a recent work based on FIR data from the Herschel Space Observatory, Santini et al. (2012) reported evidence of a higher average star formation activity in the hosts of X-ray selected AGN at $0.5 < z < 2.5$ compared to a mass-matched control sample of inactive galaxies. This enhancement is found to be higher for the most luminous AGN in the sample. However, when they only consider star-forming galaxies in the control sample, they found roughly the same level of star formation activity in the hosts of AGN and non-active galaxies.

A similar result is reported by Lutz et al. (2010), but based on submillimeter data of a sample of 895 X-ray selected sources in the Chandra Deep Field South (CDFs) and Extended-CDFS (ECDFS). The latter authors analysed stacked emission at $870 \mu\text{m}$, representative of X-ray-selected AGN at $z \sim 1$, and inferred an average SFR $\sim 31 M_\odot \text{ yr}^{-1}$, once converted to the Kroupa & Weidner (2003) IMF, and assuming star formation-dominated submillimeter emission. As claimed by Lutz et al. (2010), $30 M_\odot \text{ yr}^{-1}$ is among the typical values found for samples of non-active star-forming galaxies at $z \sim 1$ and $M_* \gtrsim 10^{10.5} M_\odot$ (e.g. Noeske et al. 2007). In fact, this value is very similar to the average SFRs reported by Rodríguez-Eugenio et al. (in prep.) and Twite et al. (2012) for samples of star forming galaxies at the same redshift and within the same range of stellar masses (see Table 7).

The star formation properties of 58 X-ray-selected AGN at $0.5 < z < 1.4$ were studied by Alonso-Herrero et al.

(2008) by modelling their multifrequency SEDs. As in the previously mentioned works, they do not find strong evidence in the host galaxies of those AGN for either highly suppressed or enhanced star formation when compared to a mass-matched sample of galaxies at the same redshifts. However, these AGN were selected to have SEDs dominated by stellar emission, and thus, they are representative of only 50% of the X-ray-selected AGN population, and likely have higher SFRs than the other half of the population.

On the other hand, Bundy et al. (2008) studied the properties of the host galaxies of X-ray selected AGN at $0.4 < z < 1.4$ in the DEEP2/Palomar survey (Bundy et al. 2006), which includes the EGS, and found a different result. They estimated the star formation quenching rate, defined as the number of galaxies that move to the red sequence per Gyr. They found that this quenching rate coincided with the AGN triggering rate, assuming an AGN lifetime of ~ 1 Gyr. Bundy et al. (2008) claimed that the agreement between the quenching and triggering rates may constitute an evidence of a physical link between the two phenomena. However, the latter authors do not consider those X-ray selected AGN the cause of the quenching, but simply that they are somehow associated to it.

Thus, by putting together all the previous results, it seems that, for X-ray selected AGN, the period of moderately luminous AGN activity may not have strong influence in the star formation activity of the galaxies. In this context, our result would be against previous evidence for moderately luminous AGN not quenching star formation. However, the majority of these works are based on the assumption that the bulk of FIR and submillimeter emission is dominated by the host galaxy (see Mullaney et al. 2011 and references therein), and they are then used as a proxy of the star formation activity. Although this may be a valid assumption in general, other authors have identified the narrow-line region clouds as the most likely location of the cool, FIR emitting dust (Dicken et al. 2009). In any case, such assumption has associated, to some degree, an overestimation the SFRs measured in AGN hosts.

An alternative scenario would be the existence of a time delay between the offset of the star formation and nuclear activity, as observed in the local universe. Davies et al. (2007) analysed the star formation in the nuclear region of nine local Seyfert galaxies on scales of 10–100 pc and found evidence for recent, but not longer active, star formation. Sampling larger scales (up to 2 kpc radius) of SDSS selected starburst

galaxies, Wild et al. (2010) found that the average rate of accretion of matter onto the black hole rises steeply ~ 250 Myr after the onset of the starburst. A similar result was found by Schawinski et al. (2009). More recently, Hopkins (2012) reported simulations of AGN fuelling by gravitational instabilities that naturally produce a delay between the peaks of SFR and nuclear activity. This offset scales as the gas consumption time and it is similar to those suggested by the observations on both small and large scales (Davies et al. 2007; Schawinski et al. 2009; Wild et al. 2010).

In order to confirm/discard the previous hypotheses, it is of extreme importance to perform accurate estimations of the AGN component to obtain reliable measurements of the SFRs in AGN hosts at $z \sim 1$ and beyond. In the future, we aim to repeat this study for a larger sample of AGN to derive statistically significant results. Considering the typical J-band magnitudes of AGN at redshift $z \sim 0.8$ (~ 20 mag), the use of 8/10 m telescopes is necessary to obtain higher signal-to-noise H α detections. The new/upcoming NIR instruments FLAMINGOS-2 on the 8 m Gemini-South and EMIR on the 10 m Gran Telescopio Canarias (GTC) will represent a definitive leap in the study of intermediate-to-high redshift AGN.

7 CONCLUSIONS

We present new NIR spectroscopic observations of a representative sample of 28 X-ray and MIR selected sources in the EGS with a median redshift of $z \sim 0.8$ ($\Delta z = [0.3, 1.3]$). These galaxies show a wide variety of SED shapes, that we use to divide the sample in AGN-dominated and host galaxy-dominated. We combined LIRIS NIR spectra with DEEP2 optical spectroscopic data to maximize the number of H α and H β detections. The main results from this study are summarised as follows:

- The NIR spectra (rest-frame optical) of the sample show a wide variety of spectral features, including prominent emission lines typical of AGN, H α and H β in absorption, weak emission lines or featureless spectra, and emission lines with double kinematic components.
- For 89% of the sample, the spectroscopic and SED classifications are in agreement, confirming the reliability of multifrequency SED fits to classify X-ray and MIR sources at intermediate redshift.
- Using different diagnostics, we can confirm the presence of nuclear activity in 24/28 sources (86%). The X-ray and MIR emission of the remaining four galaxies can be produced either by a heavily obscured low-luminosity AGN or intense star formation.
- We estimate the AGN contribution to the observed 24 μm emission using the SED fits used to classify the galaxies: 97% for *Type-1*, 72% for *Type-2*, 88% for *SB-cont*, 4% for *SB-dom*, and 25% for *NG*.
- We calculate SFRs from attenuation and AGN-corrected H α luminosities and obtain values within the interval $\text{SFR} = [0.03, 19] M_{\odot} \text{ yr}^{-1}$, which are in good agreement with the SFRs obtained from observed 24 μm fluxes: $\text{SFR} = [0.1, 166] M_{\odot} \text{ yr}^{-1}$. The average (\pm standard deviation) and median SFRs independently obtained from the two methods are $(7 \pm 7, 7) M_{\odot} \text{ yr}^{-1}$ and $(20 \pm 50, 5) M_{\odot} \text{ yr}^{-1}$ respectively.

- By comparing our results with those published in the literature for non-active star-forming galaxies of similar stellar masses and redshifts, we find that our SFRs are lower on average, although with a large dispersion. Despite the small size of the samples involved in this comparison, as well as the uncertainty affecting our AGN-corrected SFRs, the results provide an indication that the presence of an AGN in a galaxy at $z \sim 0.8$ might be quenching its star formation. Alternatively, we might be seeing a delay between the offset of the star formation and AGN activity, as observed in the local universe.

APPENDIX A: DEEP OPTICAL SPECTRA

Figures A1 to A5 show the optical spectra of the 20 galaxies in the sample with available data from DEEP2 (Davis et al. 2003). For details on how the observations were performed and other technical details, we refer the reader to Section 3.2. The flux calibration of these spectra was done by scaling them to the individual NIR LIRIS spectra.

ACKNOWLEDGMENTS

The authors acknowledge the Spanish Ministry of Science and Innovation (MICINN) through project Consolider-Ingenio 2010 Program grant CSD2006-00070: First Science with the GTC (<http://www.iac.es/consolider-ingenio-gtc/>). C.R.A. acknowledges the Estallidos group through project PN AYA2010-21887-C04.04 and STFC PDRA (ST/G001758/1). A.A.H acknowledges support from the Spanish Plan Nacional de Astronomía y Astrofísica under grant AYA2009-05705-E and from the Universidad de Cantabria through the Augusto González Linares Program.

The authors acknowledge Kevin Schawinski, Roser Pelló, Carlos González Fernández, Omaira González Martín, Guillermo Barro, Andrew Cardwell, Berto González, and Juan Carlos Guerra for their valuable help.

The authors acknowledge the data analysis facilities provided by the Starlink Project, which is run by CCLRC on behalf of PPARC.

Based on observations made with the William Herschel Telescope operated on the island of La Palma by the Isaac Newton Group in the Spanish Observatorio del Roque de los Muchachos of the Instituto de Astrofísica de Canarias under the CAT programs 18-WHT7/07B, 16-WHT7/08A, 26-WHT11/08B, and 75-WHT23/09A.

Funding for the DEEP2 survey has been provided by NSF grants AST95-09298, AST-0071048, AST-0071198, AST-0507428, and AST-0507483 as well as NASA LTSA grant NNG04GC89G.

Some of the data presented herein were obtained at the W. M. Keck Observatory, which is operated as a scientific partnership among the California Institute of Technology, the University of California and the National Aeronautics and Space Administration. The Observatory was made possible by the generous financial support of the W. M. Keck Foundation. The DEEP2 team and Keck Observatory acknowledge the very significant cultural role and reverence that the summit of Mauna Kea has always had within the

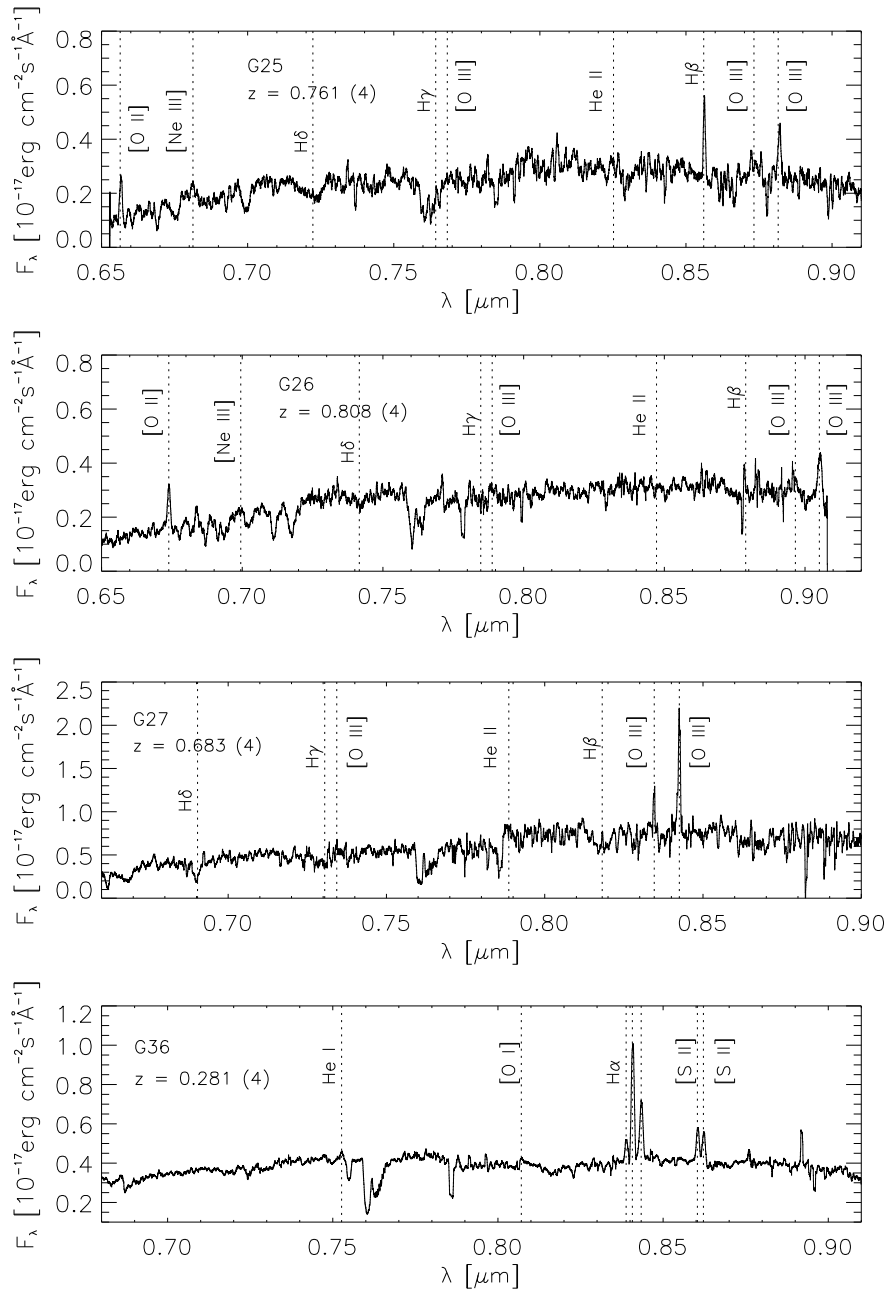


Figure A1. DEEP2 optical spectra of the galaxies G25, G26, G27, and G36. Typical AGN emission lines are labelled. The $H\alpha$ labels correspond to $H\alpha+2[N\text{ II}]$. The DEEP2 spectroscopic redshift is labelled in each panel, together with its reliability between brackets (1-2 = low and 3-4 = high reliability). **The optical spectra of all the galaxies in the sample are available in the electronic version of the journal.**

indigenous Hawaiian community and appreciate the opportunity to conduct observations from this mountain.

We finally acknowledge useful comments from the anonymous referee.

REFERENCES

Alonso-Herrero, A., Pérez-González, P. G., Rieke, G. H., Alexander, D. M., Rigby, J. R., Papovich, C., Donley, J. L., & Rigopoulou, D. 2008, *ApJ*, 677, 127

Alonso-Herrero, A. 2007, *RMxAC*, 29, 86
 Alonso-Herrero, A., et al. 2006, *ApJ*, 640, 167
 Alonso-Herrero, A., et al. 2004, *ApJs*, 154, 155
 Baldwin, J. A., Phillips, M. M., Terlevich, R. 1981, *PASP*, 93, 5
 Barmby, P., et al. 2006, *ApJ*, 642, 126
 Barro, G., et al. 2011, *ApJs*, 193, 13
 Barro, G., et al. 2009, *A&A*, 494, 63
 Bauer, F. E., Yan, L., Sajina, A., Alexander, D. M. 2010, *ApJ*, 710, 212
 Bicker, J., Fritze-v. Alvensleben, U. 2005, *A&A*, 443, L19

- Bolzonella, M., Miralles, J.-M., & Pelló, R. 2000, *A&A*, 363, 476
- Boyle, B. J., McMahon, R. G., Wilkes, B. J., Elvis, M. 1995, *MNRAS*, 276, 315
- Brusa, M., et al. 2009, *A&A*, 507, 1277
- Bundy, K., et al. 2008, *ApJ*, 681, 931
- Bundy, K., et al. 2006, *ApJ*, 651, 120
- Calzetti, D., et al. 2007, *ApJ*, 666, 870
- Cardelli, J. A., Clayton, G. C., & Mathis, J. S. 1989, *ApJ*, 345, 245
- Chabrier, G. 2003, *PASP*, 115, 763
- Cohen, J. G., Hogg, D. W., Blandford, R., Cowie, L. L., Hu, E., Songaila, A., Shopbell, P., & Richberg, K. 2000, *ApJ*, 538, 29
- Davies, R. I., Müller Sánchez, F., Genzel, R., Tacconi, L. J., Hicks, E. K. S., Friedrich, S., Sternberg, A. 2007, *ApJ*, 671, 1388
- Davis, M., et al. 2007, *ApJ*, 660, 1
- Davis, M., et al. 2003, *Proc. SPIE*, 4834, 161
- Dicken, D. Tadhunter, C., Axon, D., Morganti, R., Inskip, K. J., Holt, J., González Delgado, R., & Groves, B. 2009, *ApJ*, 694, 268
- Doherty, M., Bunker, A., Sharp, R., Dalton, G., Parry, I., Lewis, I. 2006, *MNRAS*, 370, 331
- Doherty, M., et al. 2004, *MNRAS*, 354, L7
- Dutton, A. A., van den Bosch, F. C., & Dekel, A. 2010, *MNRAS*, 405, 1690
- Faber, S. M., et al. 2003, *Proc. SPIE*, 4841, 1657
- Ferrarese, L., et al. 2006, *ApJ*, 644, L21
- Ferrarese, L., Merritt, D. 2000, *ApJ*, 539, L9
- Fiore, F., et al. 2012, *A&A*, 537, 16
- Gallego, J., Zamorano, J., Aragón-Salamanca, A., Rego, M. 1995, *ApJ*, 455, L1
- Gebhardt, K., Bender, R., Bower, G., et al. 2000, *ApJ*, 539, L13
- Georgakakis, A., et al. 2006, *MNRAS*, 371, 221
- Granato, G. L., De Zotti, G., Silva, L., Bressan, A. & Danese, L. 2004, *ApJ*, 600, 580
- Greene, J. E. & Ho, L. C. 2006, *ApJ*, 641, L21
- Groth, E. J., et al. 1994, *BAAS*, 26, 1403
- Gwyn, S. D. J. 2012, *AJ*, 143, 38
- Ho, L. C. 2005, *ApJ*, 629, 680
- Homeier, N. L., Gallagher, J. S. 1999, *ApJ*, 522, 199
- Hopkins, P. F. 2012, *MNRAS*, 420, L8
- Horne, K. 1986, *PASP*, 98, 609
- Kauffmann, G., et al. 2003, *MNRAS*, 346, 1055
- Kennicutt, R. C., et al. 2009, *ApJ*, 703, 1672
- Kennicutt, R. C. 1998, *ARA&A*, 36, 189
- Kewley, L. J., Groves, B., Kauffmann, G., & Heckman, T. 2006, *MNRAS*, 372, 961
- Kewley, L. J., Dopita, M. A., Sutherland, R. S., Heisler, C. A., Trevena, J. 2001, *ApJ*, 556, 121
- Kormendy, J., Richstone, D. 1995, *ARA&A*, 33, 581
- Kroupa, P. & Weidner, C. 2003, *ApJ*, 598, 1076
- Lilly, S. J., Hammer, F., Le Fevre, O., & Crampton, D. 1995, *ApJ*, 455, 75
- Lutz, D. et al. 2010, *ApJ*, 712, 1287
- Magnelli, B., et al. 2010, *A&A*, 518, L28
- Magorrian, J., et al. 1998, *AJ*, 115, 2285
- Manchado, A., et al. 2004, *Proc. SPIE*, 5492, 1094
- Mullaney, J. R., Alexander, D. M., Goulding, A. D., & Hickox, R. C. 2011, *MNRAS*, 414, 1082
- Nandra, K., et al. 2005, *MNRAS*, 356, 568
- Newman, J. A., et al. 2012, *ApJs*, submitted, arXiv:1203.3192
- Noeske, K. G., et al. 2007, *ApJ*, 660, L43
- Pereira-Santaella, M., et al. 2011, *A&A*, 535, 93
- Pérez-González, P. G., Trujillo, I., Barro, G., Gallego, J., Zamorano, J., & Conselice, C. J. 2008, *ApJ*, 687, 50
- Piccinotti, G., Mushotzky, R. F., Boldt, E. A., Holt, S. S., Marshall, F. E., Serlemitsos, P. J., & Shafer, R. A. 1982, *ApJ*, 253, 485
- Polletta, M. et al. 2007, *ApJ*, 663, 81
- Osterbrock, D. 1989, *Astrophysics of Gaseous Nebulae and Active Galactic Nuclei*. University Science Books, Mill Valley, California.
- Ramos Almeida, C., Rodríguez Espinosa, J. M., Barro, G., Gallego, J., Pérez-González, P. G. 2009, *AJ*, 137, 179
- Ranalli, P., et al. 2012, *A&A*, 542, 16
- Ranalli, P., Comastri, A., Setti, G. 2003, *A&A*, 399, 39
- Rieke, G. H., Alonso-Herrero, A., Weiner, B. J., Pérez-González, P. G., Blaylock, M., Donley, J. L., & Marcillac, D. 2009, *ApJ*, 692, 556
- Rigby, J. R., Rieke, G. H., Donley, J. L., Alonso-Herrero, A., Pérez-González, P. G. 2006, *ApJ*, 645, 115
- Risaliti, G., Maiolino, R., Salvati, M. 1999, *ApJ*, 522, 157
- Salpeter, E. E. 1995, *ApJ*, 121, 161
- Santini, P., et al. 2012, *A&A*, 540, 109
- Schawinski, K., et al. 2009, *ApJ*, 690, 1672
- Schawinski, K., et al. 2007, *MNRAS*, 382, 1415
- Schneider, D. P., et al. 2005, *AJ*, 130, 367
- Springel, V., Di Matteo, T., & Hernquist, L. 2005, *MNRAS*, 361, 776
- Steidel, C. C., Adelberger, K. L., Shapley, A. E., Pettini, M., Dickinson, M., Giavalisco, M. 2003, *ApJ*, 592, 728
- Trump, J. R., et al. 2009, *ApJ*, 706, 797
- Twite, J. W., Conselice, C. J., Buitrago, F., Noeske, K., Weiner, B. J., Acosta-Pulido, J. A., Bauer, A. E. 2012, *MNRAS*, 420, 1061
- Vacca, W. D., Cushing, M. C., & Rayner, J. T. 2003, *PASP*, 115, 389
- Villar, V., Gallego, J., Pérez-González, P. G., Barro, G., Zamorano, J., Noeske, K., & Koo, D. C. 2011, *ApJ*, 740, 47
- Waskett, T. J., Eales, S. A., Gear, W. K., McCracken, H. J., Brodwin, M., Nandra, K., Laird, E. S., Lilly, S. 2004, *MNRAS*, 350, 785
- Wehner, E. H. & Harris, W. E. 2006, *ApJ*, 644, L17
- Westmoquette, M. S., Smith, L. J., Gallagher, J. S. 2011, *MNRAS*, 414, 3719
- Wild, V., Heckman, T., Charlot, S. 2010, *MNRAS*, 405, 933